

# Estimation of Blood Pressure and Perfusion Rates with Ultrasound and Photoacoustic Imaging

by

Min Choi

A thesis submitted in partial fulfillment of the requirements for the  
degree of

Master of Science

in

Biomedical Engineering

Department of Electrical and Computer Engineering

University of Alberta

©Min Choi, 2018

# Abstract

Being able to characterize and assess hemodynamics in patients is regarded as essential in understanding vascular and tissue health for diagnostic purposes. There are many parameters associated with hemodynamics such as intravascular pressure, flow rates and perfusion rates, which are important in conditions such as atherosclerosis, ulcers, ischemia, and cancer. Standardized clinical methods have been established to assess some of these properties. Nevertheless, there are limitations to these techniques. Specifically, there are no suitable non-invasive methods to measure blood pressure in small vessels nor to assess the status of perfusion of microvasculature in deep tissues without contrast agents. This thesis introduces methods of using photoacoustic-ultrasound dual imaging technique to provide a label-free and non-invasive method to quantify blood pressures in micro-vessels and re-perfusion rates in subsurface tissue regions. When a compressive force is applied to a section of an arm of a patient, the cross-sectional lumen area of vessels decrease as the force increases eventually causing them to collapse. The change in the area is detected by photoacoustic imaging and the applied pressure is measured synchronously. The internal pressure is estimated by fitting the detected area and pressure onto a mathematical model. The extent of the model's use is further investigated by fitting the model to a

data obtained from simulations of finite element models of thick-walled tube and a human arm. Additional mathematical models, one derived from constitutive equations and another modified from the original fitting model are also used to fit the models to a simulated data for comparisons and to find the extent of their applicability with different loading processes. We also show methods to estimate re-perfusion rates through photoacoustic-ultrasound dual imaging. To maintain the region of interest where re-perfusion is being tracked, the amount of displacement during compression is estimated by ultrasound displacement tracking algorithm. This is used to show the estimation of re-perfusion rates for tissues in the subsurface regions. This thesis aims to introduce and investigate these estimation methods that may have potential application for diagnostic purposes.

# Preface

This thesis is an original work by Min Choi. The research project, of which this thesis is a part, received research ethics approval from the University of Alberta Research Ethics Board, Pro00007759.

The introduction in chapter 1, the background information in chapter 2 and the final concluding chapter are all my original work.

Chapter 3 has been published as M. Choi; R. Zemp. "Relative Microvascular Pressure Sensing" Proc. SPIE 9708, Photons Plus Ultrasound: Imaging and Sensing 2016; 97081D (2016); doi: 10.1117/12.2213607. I was responsible for the entire work including setting up and performing experiments, analysis and writing of the manuscript. R. Zemp was the supervisory author and was involved with conceptual development and manuscript preparation.

Chapter 4 has been published as M. Choi; R. Zemp. "Compression-tracking photoacoustic perfusion and microvascular pressure measurements", Proc. SPIE 10064, Photons Plus Ultrasound: Imaging and Sensing 2017; 100643R (2017); doi: 10.1117/12.2253287. I was responsible for the entire work including setting up and performing experiments, analysis and writing of the manuscript. R. Zemp was the supervisory author and was involved with conceptual development and manuscript preparation.

Chapter 5 has been published as M. Choi; A. M. J. Shapiro; R. Zemp. "Tissue perfusion rate estimation with compression-based photoacoustic-ultrasound imaging", *Journal of Biomedical Optics* 23.01 (2018) p.1-8 ISSN: 1560-2281, DOI: 10.1117/1.JBO.23.1.016010. I was responsible for the entire work including setting up and performing experiments, analysis and writing of the

manuscript. R. Zemp was the supervisory author and was involved with conceptual development and manuscript preparation.

## Acknowledgements

We gratefully acknowledge funding from NSERC (RGPIN 355544, 494293-16, 375340-2009, STPGP 396444, EQPEQ 440290, EQPEQ 423474, EQPEQ 423197), CIHR (PS 153067, CPG 134739), Canadian Cancer Society (CCS 2011-700718, CCS 702032), Prostate Cancer Canada (PCC MVBRDG D2013-40), and Alberta Innovates Health Solutions (CRIO TEAM).

I would like to express my sincere gratitude to my supervisor, Dr. Roger Zemp whom I had the pleasure of working since my undergraduate studies. In addition, I would like to thank my past and present colleagues, Wei Shi, Alexander Forbrich, Ryan Chee and Quinn Barber, some of whom have introduced and guided me in learning essential techniques required for my project, and others whom have provided technical assistance in performing experiments for many hours.

I would also like to thank my thesis supervisory committee, Dr. Samer Adeeab for providing his insight on the finite element simulation portion of my project, and Dr. Ray Decorby for his time and insight on my thesis project.

Finally, I would like to thank my family for their continuing unconditional support and encouragement.

# Contents

<b>Abstract</b>	<b>ii</b>
<b>Preface</b>	<b>iv</b>
<b>Acknowledgements</b>	<b>vi</b>
<b>Contents</b>	<b>vii</b>
<b>List of figures</b>	<b>x</b>
<b>List of Tables</b>	<b>xiii</b>
<b>1 Introduction</b>	<b>1</b>
1.1 Motivation . . . . .	2
1.2 Scope of the thesis and key contributions . . . . .	4
1.3 Organization of Thesis . . . . .	6
<b>2 Background</b>	<b>9</b>
2.1 Ultrasound Wave Propagation Theory . . . . .	9
2.2 Ultrasound Imaging . . . . .	11
2.3 Applications of Ultrasound Imaging . . . . .	13
2.3.1 Doppler Ultrasound Imaging . . . . .	13
2.3.2 Contrast Enhanced Ultrasound Imaging . . . . .	15
2.3.3 Strain Elastography . . . . .	17
2.4 Photoacoustic Effect . . . . .	19
2.5 Photoacoustic Imaging . . . . .	20
2.5.1 Functional Photoacoustic Imaging . . . . .	23
2.6 Other Pre-clinical and Clinical Perfusion Imaging Systems . . . . .	24
2.6.1 MRI . . . . .	24

2.6.2	Computed Tomography . . . . .	25
2.6.3	Positron Emission Tomography . . . . .	25
2.6.4	Laser Speckle Imaging . . . . .	25
2.6.5	Nailfold Capillaroscopy . . . . .	26
2.6.6	Near-Infrared Spectroscopy . . . . .	26
2.6.7	Reflectance Spectroscopy . . . . .	27
2.7	Deformation of Vessels Due to External Load . . . . .	27
<b>3</b>	<b>Relative Microvascular Pressure Sensing</b>	<b>31</b>
3.1	Introduction . . . . .	32
3.2	Phantom Experiment . . . . .	33
3.2.1	Experimental Setup . . . . .	33
3.2.2	Results and Limitations . . . . .	33
3.3	<i>In Vivo</i> Experiment . . . . .	35
3.3.1	Experimental Setup . . . . .	35
3.3.2	Vessel Tracking Algorithm . . . . .	36
3.3.3	Results and Discussions . . . . .	37
3.3.4	Conclusion . . . . .	38
<b>4</b>	<b>Compression-tracking photoacoustic perfusion and microvascular pressure measurements</b>	<b>41</b>
4.1	Introduction . . . . .	41
4.2	Methods . . . . .	43
4.3	Microvascular Pressure Measurement . . . . .	43
4.4	Compression-Reperfusion Rate Estimation . . . . .	44
4.5	Conclusion . . . . .	46
<b>5</b>	<b>Perfusion Rates Tracking</b>	<b>47</b>
5.1	Introduction . . . . .	47
5.2	Methods . . . . .	50
5.2.1	Imaging System . . . . .	50
5.2.2	Human Subject Imaging Study . . . . .	51
5.2.3	Analysis Method . . . . .	53
5.3	Results . . . . .	54
5.4	Discussion . . . . .	57

5.5	Additional Discussion . . . . .	62
5.6	Conclusions . . . . .	62
<b>6</b>	<b>Estimation of Vessel Internal Pressures with Tissue Deformation</b>	<b>65</b>
6.1	Introduction . . . . .	65
6.2	Finite Element Model Description . . . . .	66
6.2.1	Geometry . . . . .	67
6.3	Fitting Models . . . . .	69
6.4	Fitting Methods . . . . .	70
6.5	Results . . . . .	71
6.5.1	Thick-walled Tube with Uniform Loading . . . . .	71
6.5.2	Centered Vessel With Top Loading . . . . .	74
6.5.3	Arm Model with Uniform Loading . . . . .	75
6.5.4	Arm Model with Top Loading . . . . .	76
6.6	Discussion . . . . .	76
<b>7</b>	<b>General Discussion, Future Work and Conclusion</b>	<b>85</b>
7.1	Discussion . . . . .	85
7.2	Future Work . . . . .	87
7.3	Conclusion . . . . .	88
	<b>Bibliography</b>	<b>90</b>
<b>A</b>	<b>Derivation of The Quadratic Model</b>	<b>107</b>

# List of Figures

2.1	A basic schematic of photoacoustic effect. In a clinical setting, medium 1 is often ultrasonic gel or water and medium 2 is soft tissue . . . . .	20
2.2	Changes in the Normalized Area and the Shape of a Vessel with Changes in the Transmural Pressure [6] . . . . .	28
3.1	A basic schematic of the compression experiment. The transducer surface (gray) compresses on the phantom (yellow) surface directly. The phantom is submerged in water (blue) to provide impedance matching. A scale (not shown) is placed below the phantom to measure the applied pressure. . . . .	34
3.2	Case 1 (left): The vessel compresses and the top and the bottom of the vessel can no longer be differentiated, however, the signal does not vanish even when the load double after signal merges. Case 2 (right): The vessel completely vanishes after the transmural pressure reaches a critical value. The flow stoppage is visualized for both cases. . . . .	34
3.3	Compression of the transducer on the thin chicken breast tissue. The flow rate corresponds to the internal pressure which is set by the syringe pump and the measured mass is the value shown on the scale at which the vessels close. The measured mass corresponds to the external pressure. . . . .	36
3.4	(a): The <i>in vivo</i> experimental setup. (b): The capacitive sensor can measure both compression and tension. When the transducer is hanging in mid-air, the sensor is being pulled down, which will be considered as the zero point (tare value). . . . .	37

3.5	(A) The synchronization between imaging and the force sensing. (B) The tracking and color coding of four vessels, three vessels disappear at similar time and the coded colors are similar. The vessels are detected only up to where the signals disappear . . .	39
4.1	Schematic of Force Detection and US-PA Dual Imaging . . . . .	42
4.2	Different Stages of Vessel Buckling Due to Increasing External Pressure . . . . .	44
4.3	(Large) Fit of Multiple Pressure-Area Curve for a Single Venule. (Small) Zoomed in Data Fit of Second Compression. . . . .	44
4.4	Change in Total PA Signal with Applied External Pressure on a Forearm Submerged in an ice-bath and the Curve Fitted to the Total PA Signal According to the Equation shown above a) 1 min. in an ice-bath b) 2 min. in an ice-bath . . . . .	46
5.1	PA signals of the blood before and during full compression . . .	52
5.2	a) location of the transducer on the hand, b) the transducer fixed on the top along with the force sensor. The transducer and the force sensor are restricted to a vertical movement and c) an example of PA signal tracking synchronized with pressure sensor reading . . . . .	52
5.3	Schematic of reperfusion rate analysis: a) placement of the ROI and sliding window in the initial frame and the warping of the sliding window that correlates to the tissue movement. b) Overview of how PA signals are measured and tracked over multiple frames.	55
5.4	The Transformation of a Sliding Window a) During Slight Relaxation and b) Full Relaxation Using Displacement Estimated by AM2D. The small plots within the large plots are magnified version of the large plot. . . . .	56
5.5	The re-fill rate distribution of the left hand of a human subject in the a)-c) 4°C water bath for 30s, 60s and 90s respectively and d)-f) 45°C water bath for 0s, 30s and 60s respectively. Times shown above each image denote the exposure time at the start of each C-R cycle. The size of sliding window is 4.24 mm wide and 0.78 mm long . . . . .	58

5.6	The average perfusion rates with different sliding window sizes as a function of exposure time in the hot- and cold water baths. Sub-figures are for the following initial sliding window sizes. a) 4.24 mm by 0.78 mm b) 2.83 mm by 0.78 mm, c) 1.41 mm by 0.78 mm and d) 0.83 mm by 1.95 mm . . . . .	59
6.1	The dimensions of the cross-sections of (A) tube wall model and (B) human arm model, z-axis is directed out-of-page . . . . .	68
6.2	Various views of the Four Simulation Models . . . . .	69
6.3	A sample of fitting on results from FEM simulation of a thick-walled tube. . . . .	72
6.4	A sample of fitting on results from FEM simulation of a thick-walled tube. . . . .	72
6.5	Data Fitting using Quadratic Model on a Small Strain Region with Young's modulus of 40 kPa . . . . .	73
6.6	A sample of fitting on results from FEM simulation of a thick-walled tube using a quadratic model. . . . .	74
6.7	A sample of fitting on results from FEM simulation of a thick-walled tube using a quadratic model. . . . .	80
6.8	Data Fitting using Quadratic Model on a Small Strain Region with Young's modulus of 40 kPa . . . . .	81
6.9	A sample of fitting on results from FEM simulation of a thick-walled tube using a modified exponential model. . . . .	82
6.10	A sample of data fitting on the arm model using the quadratic model . . . . .	83
6.11	A sample of the goodness of the fit on results from FEM simulation of an arm model using a quadratic model. . . . .	84

# List of Tables

4.1	Estimated Kappa and Internal Pressure of a Single Venule . . .	45
5.1	The estimated mean re-fill rates. The submersion time is the duration the hand was submerged in a water bath before the start of the compression . . . . .	58
6.1	A sample of comparison between the parameters used in the simulations and the estimated parameters by curve fitting using exponential model for the data in the post-buckling region . . . . .	79
6.2	A sample of comparison between the parameters used in the simulations and the estimated parameters by curve fitting using modified exponential model for the data in the pre-buckling region . . . . .	79
6.3	A sample of comparison between the parameters used in the simulations and the estimated parameters by curve fitting using quadratic model for the data in the small-strain region . . . . .	80
6.4	A sample of comparison of internal pressures between one set by FEM and others estimated by different models . . . . .	81
6.5	A sample of comparison between the parameters used in the simulations and the estimated parameters by curve fitting using quadratic model for the data in the small-strain region . . . . .	82
6.6	A comparison of parameters (A) set on FEM and (b) estimated using the quadratic model . . . . .	83
6.7	A comparison of parameters (A) set on FEM and (B) estimated using quadratic model . . . . .	84



# Chapter 1

## Introduction

Tissue perfusion and pressure in the microcirculation are critical parameters of interest for a wide range of diseases including diabetes, pressure ulcers, atherosclerosis, tissue ischemia, cancer, and various cardiovascular diseases. However, methods to estimate perfusion and microvascular pressure are very limited. In particular, there are no non-invasive methods for estimating intravascular pressure in small vessels. Having even approximate or relative measures of such pressures could help clinicians understand origins and consequences of disease.

There is an unmet need of improved tools to inform doctors of severity of ischemia which impacts clinical decisions. For example, diabetic patients with severe ulcers may require amputation. This represents a life-changing event and comes with heavy economic and social consequences. Improved methods to detect ischemia early and to monitor efficacy of therapeutic interventions is urgently needed. If complications can be caught early and remedied, not only billions of dollars could be saved potentially due to reduced amputations, it can also allow accurate diagnosis that ultimately leads to increase in rates of patient survival and recovery.

Angiogenesis (the growth of new blood vessels) is a hallmark of cancer and some other diseases. It is accompanied by vascular dysregulation resulting in abnormal perfusion. Sometimes necrotic hypoxic tumor cores develop with quiescent cells which can rebound with aggressiveness. Being able to estimate

perfusion in and around tumors could prove as an important predictor of tumor aggressiveness. Hypoxic tumors are sometimes more resistant to radiation and chemotherapy. Therefore, improved tools to image hypoxia, perfusion and microvascular pressures could help predict tumor response to therapy and provide monitoring tools for therapy efficacy. Such tools may enable improved clinical decision making, perhaps opting for more up-front aggressive therapies when it is thought that more moderate therapies may be ineffective.

This thesis represents a step on the journey to develop tools to address these unmet needs. In brief, we develop novel ultrasound and photoacoustic imaging methods for estimating tissue perfusion non-invasively, and provide methods for estimating relative pressures in small vessels. In this chapter, we provide further information about motivation, then explain the contributions of this thesis and explain the content of forthcoming chapters.

## 1.1 Motivation

The microcirculatory system in the human body governs the delivery of nutrients and oxygen to tissues throughout the entire body. Alteration of the system from the normal physiological condition can be caused by diabetes, smoking, hypertension, trauma, abnormally high or low blood pressure, genetic abnormalities, hyperlipidemia and more [1, 2]. These causes can be either acute or chronic, which results in an accurate diagnosis or prevention to be difficult.

In the peripheral region, circulatory disorders can appear in forms of cancer, pressure and vascular ulcers among others as cancer cells impair blood flow in the capillary networks due to tumor angiogenesis and ulcers cause ischemia in the blood vessel networks due to lipid or calcium occlusion [3, 4]. Such symptoms can cause dramatic changes in vascular properties such as blood pressure, flow and perfusion rates and vessel structures.

---

Between 1990 and 2013, the mortality caused by peripheral vascular disease have increased by more than 150% [5]. With the change of more sodium-concentrated diet and sedentary lifestyle, vascular disease, while not limited to peripheral regions, is becoming increasingly prominent. A rough way of assessing peripheral vascular health involves, palpating and visually inspecting the areas that are thought to have abnormalities such as varicose veins, ulcers and other deformities. More accurate methods for assessment include estimating perfusion rates and monitoring blood pressure, blood flow, oxygen saturation, local body temperature, and respiratory rate among others.

Assessing blood pressure in small vessels is difficult. Currently most methods are meant for assessing pressure in large vessels. Two methods currently used in clinics to measure blood pressure include: (1) an invasive method that employs catheterization, which allows small catheters or cannulae needles to be inserted into major veins, arteries or heart chamber to monitor the blood pressure continuously. (2) A non-invasive method is to use sphygmomanometer by wrapping a pressure cuff around a person's upper arm to measure systemic arterial blood pressure. However, measuring blood pressure of small vessels such as arterioles, venules and capillaries are not yet possible due to its small size and lack of pulsatility. Therefore, only various imaging techniques have been used to make diagnostic decisions for those vessels. One way to estimate internal pressure of vessels is to understand and model how applying external pressure affects the cross-sectional area of vessels. While there were experiments for such purpose in both *ex vivo* and *in vivo* cases, the extent of applicability of derived mathematical models from some of the experiments are unknown [6, 7, 8].

Apart from measuring blood pressure, characterizing perfusion has been a topic of intense research. In clinics, perfusion imaging, which translates the perfusion rates on a color intensity map, has been performed using MRI, CT, PET and ultrasound [9, 10, 11]. However, methods of measuring perfusion

rates lack standardized protocols, and require contrast agents which preclude their use for screening purposes. There is also way to measure perfusion rates in very superficial tissues based on laser speckle imaging, which is cheaper than MRI and uses non-ionizing radiations unlike CT and PET [12]. However, the depth is severely limited due to light scattering and this method cannot be compared with other perfusion imaging methods as the obtained perfusion rates are not yet highly quantitative.

## 1.2 Scope of the thesis and key contributions

This thesis investigates the potential of ultrasound and photoacoustic imaging for imaging blood perfusion rates and for estimating intravascular pressure in small vessels where traditional cuff approaches cannot be used. Photoacoustic imaging is an emerging hybrid modality which uses pulsed laser light to excited sub-surface optical absorbers. Absorbed light induces thermo-elastic expansion to produce photoacoustic signals which are detected by an ultrasound transducer and reconstructed to form images with optical absorption contrast and ultrasonic spatial resolution, even at depths where light scattering would otherwise render pure optical approaches incapable of resolving small structures. Photoacoustic imaging has previously been used for visualization of microvascular networks, however, it has not yet been used for estimating tissue perfusion. Perfusion is the net rate of blood exchange per unit tissue volume. Other approaches for quantitatively imaging perfusion rates require contrast agents. The proposed approach is completely label free. Our approach involves compressing tissue to exclude blood flow then imaging the re-establishment of perfusion and estimating the wash-in rates for image location. These methods and results are detailed in Chapter 5 and represent the first approach to contrast-agent free perfusion-rate imaging, to the best of our knowledge.

---

Additionally, we investigate non-invasive imaging approaches to estimate pressure in small vessels. The initial hypothesis was that when an externally applied pressure overcomes internal blood pressures, vessels would collapse, and exclude blood flow. This loss of blood signal in photoacoustic images was tracked over multiple frames during tissue compression and relative pressure maps were generated using tracking algorithms and measured externally applied forces. This work represents the first demonstration of relative pressure imaging in microvessels.

Further investigation revealed that the relationship between externally applied forces and internal pressures was significantly more complicated than originally anticipated. An alternative approach was conjectured to potentially enable quantitative internal pressure estimation. This approach involved tracking the cross-sectional area of vessels as a function of applied external pressure. The curve of normalized cross-sectional area as a function of this external loading was fit to three potential models of vessel deformation. One model was used to fit experimental photoacoustic data to estimate internal pressures in small vessels in a human subject. However, no validation was possible. Nevertheless, this work represents the first attempt and quantifying microvascular pressures *in vivo*.

With an aim to produce model validation, Finite Element simulations were performed which mimic vessels in tissue models. Data from finite element simulations were then fit using proposed analytical deformation models to extract parameters including internal pressures and in some cases tissue mechanical properties. The successes and limitation of these attempts are detailed in Chapter 6. Key contributions detail limitations of previous models and outline new models more applicable to *in vivo* settings.

### 1.3 Organization of Thesis

- Chapter 2 provide background on ultrasound and photoacoustic imaging, as well as current methods for tissue perfusion imaging and vascular pressure estimation including their deficiencies and unmet needs.
- Chapter 3 introduces a method for performing photoacoustic imaging on a flow phantom while measuring the applied pressure synchronously and in real-time. This chapter was published as M. Choi; R. Zemp. "Relative Microvascular Pressure Sensing" Proc. SPIE 9708, Photons Plus Ultrasound: Imaging and Sensing 2016; 97081D (2016); doi: 10.1117/12.2213607.
- Chapter 4 is a two-part experiment where the first part attempts to qualitatively define blood pressure of small vessels in relations to each other and the second part is to use the same experimental setup to measure and quantify reperfusion rates. This chapter was published as M. Choi; R. Zemp. "Compression-tracking photoacoustic perfusion and microvascular pressure measurements", Proc. SPIE 10064, Photons Plus Ultrasound: Imaging and Sensing 2017; 100643R (2017); doi: 10.1117/12.2253287.
- Chapter 5 is a work on establishing a method of measuring and quantifying reperfusion rate in superficial tissue region non-invasively using photoacoustic-ultrasound dual imaging. This chapter has been published as M. Choi; A. M. J. Shapiro; R. Zemp. "Tissue perfusion rate estimation with compression-based photoacoustic-ultrasound imaging", *Journal of Biomedical Optics* 23.01 (2018) p.1-8 ISSN: 1560-2281, DOI: 10.1117/1.JBO.23.1.016010
- Chapter 6 explores the applicability of various mathematical models in detecting changes of cross-sectional lumen area of a vessel due to external loading.

A concluding chapter summarizes work done and discusses successes and limitations, while outlining potential future work.



## Chapter 2

# Background

Given that this thesis involves work in ultrasound and photoacoustic imaging, tissue motion tracking, perfusion estimation, and vessel pressure estimation, significant background is required in variety of areas. In this chapter we present some background information important for understanding key contributions of the thesis. We begin by including some fundamentals of ultrasound theory and imaging. We briefly review some ultrasound applications and highlight previous work on Doppler blood flow imaging, ultrasound contrast agent imaging, and strain imaging. This background information on ultrasound is important for understanding our contributions which use ultrasound to estimate tissue motion. We then introduce the photoacoustic effect and give a brief overview of photoacoustic imaging methods. Methods for assessing perfusion rates are then discussed followed by background on vessel deformation, needed for future chapters discussing pressure estimation.

### 2.1 Ultrasound Wave Propagation Theory

Ultrasound is defined as acoustic waves with frequency above 20 kHz. It propagates as longitudinal waves through media such as air, water, and tissue but can also exist in the form of a shear wave in non-gaseous media. The speed of sound,  $c$ , is dependent on the material property, which is calculated by the following expression  $c = \sqrt{\frac{1}{k\rho}}$ , where  $k$  is the material compressibility and  $\rho$  is

the material density. Similar to a simple electrical circuit, ultrasound wave also behaves differently depending on material type, which is known as the acoustic impedance. The acoustic impedance,  $Z$ , can be expressed as  $Z = \rho c$ .

As acoustic waves travel in a medium, pressure amplitude will decrease exponentially due to the continuous acoustic absorption and scattering as it collides with molecules. The combined effects are known as attenuation. The attenuations in materials are complex as they are non-linear and frequency dependent. For soft tissue, attenuations can be estimated by an expression  $\alpha = \alpha_0 f^n$ , where  $\alpha_0$  is the temperature dependent factor,  $f$  is the frequency and  $n$  is defined by the material parameter that is between 1 and 2 for soft tissue. Due to the attenuation the acoustic wave amplitude decay can be defined as  $A(z) = A_0 e^{-\alpha(z)z}$ , where  $A_0$  is the original acoustic amplitude and  $z$  is the distance traveled by the wave in a medium.

When longitudinal waves travel from one isotropic medium to another with a smooth interface, the angle of incidence on the interface and the difference in acoustic impedance causes transmitted wave to both reflect and refract. The material properties and the incident angle determines the angles of reflection and transmittance and their respective wave amplitudes. The relationship between angles of incidence, reflectance and transmission are governed by the law of reflection and Snell's Law, which can be expressed as  $\theta_i = \theta_r$  and  $\frac{\sin \theta_i}{\sin \theta_t} = \frac{c_i}{c_t}$ , where  $\theta_i$  is the angle of incidence,  $\theta_r$  is the angle of reflectance,  $\theta_t$  is the angle of transmission,  $c_i$  is the speed of sound in the incident medium and  $c_t$  is the speed of sound in the transmitted medium. Also according to Snell's law, there exists a critical angle, expressed below, for which, in the case where the angle of incidence is greater than the critical angle, the acoustic wave will be reflected completely with no energy loss. The critical angle,  $\theta_{cr}$  is equivalent to  $\arcsin(\frac{c_i}{c_t})$ ,  $c_i < c_t$ . Therefore when acoustic waves travel across

from one medium to another, the reflection coefficient and transmission coefficient of the pressure wave intensity can be expressed as  $R = \frac{Z_t \cos \theta_i - Z_i \cos \theta_t}{Z_t \cos \theta_i + Z_i \cos \theta_t}$  and  $T = \frac{2Z_t \cos \theta_i}{Z_t \cos \theta_i + Z_i \cos \theta_t}$ , where  $Z_i$  and  $Z_t$  are the acoustic impedance of the media for the incident and transmitted wave respectively.

## 2.2 Ultrasound Imaging

Ultrasound imaging is a clinical tool used for many decades. Its characteristics are marked by small size, low-cost, non-invasiveness and safety. In addition, ultrasound imaging has a wide range of clinical applicability, which includes anesthesiology, angiology, cardiology, gastroenterology, gynecology, neonatology, neurology, obstetrics, ophthalmology, urology, cardiovascular system, surgery guidance imaging to name a few. Its wide usage is derived from various characteristics that determine imaging system qualities such as bandwidth frequency, pulse repetition rate, pulse energy and beamforming and tomographic techniques. Application of ultrasound is not only limited to imaging but extends to clinical treatments. For example, high-intensity focused ultrasound (HIFU) is a pre-clinical method to treat malignant tissue cells non-invasively by ablation [13].

When acoustic waves are transmitted from an ultrasound transducer, it comes in contact with the layer of imaging sample and produces a reflecting wave, an "echo", where it is received by the same or a different transducer. The received signal is then used for image reconstruction. Choosing a suitable imaging transducer depends on the frequency-dependent material characteristics and thickness of the imaging sample. One of the common issues in ultrasound imaging is the heterogeneity of the imaging materials. For instance, sound waves traveling in an acoustically heterogeneous material experience multiple speeds depending on the material composition, which may cause systematic error in image reconstruction as the speed of sound is treated as a constant in many

imaging systems. In soft tissues imaging, the change in the speed of sound due to heterogeneity is largely ignored as it is negligible ( $< 5\%$ ) compared to the actual speed (1540 m/s). However, difference in wave speeds can be exploited to determine body compositions such as bone density, body fat and muscle thickness [14, 15, 16].

The imaging system is characterized by a number of properties such as bandwidth frequency, the transmission frequency, focusing, electronic control, numerical aperture and a number of other aspects. Usually, the transmission frequency of the transducer is the center frequency, and image depth and axial resolution are dependent by the the bandwidth frequency of the imaging transducer, while the lateral resolution and elevation resolution are limited by the beam width and thickness. In clinical ultrasound, frequency range of 1- 18 MHz are used while higher frequency transducers ( $> 18$  MHz) are used for pre-clinical trials and experimental studies. The range of frequency used in clinical ultrasound provides imaging depth in the order of multiple cm and is capable of imaging kidneys, livers and fetus, which are located deep within the body, albeit with low resolutions. In comparison, higher frequency can be used to image breast, muscle, superficial tissue, dermal vascular structures as they are closer to the skin surface and it provides higher resolution.

Images can be formed from received signals using various techniques and methods. When a single transducer element receives a signal for a specific duration, it forms an "A-scan", which is a line image that can be interpreted as a representation of the signal envelope over time. The time-of-flight between a transmission and echo of acoustic signal determines the image depth. With multiple A-scans lined up side by side, it forms a 2D image, which is called the B-scan. A most basic example of transducer capable of forming B-scans are linear array transducers that is made of multiple transducers elements placed in a line. With transducer arrays, both the design and the beamforming technique

can be used to achieve better image resolution and quality. Design-wise, the transducer array can be convex to cover a larger field of view or concave that can create a natural focal zone. In addition, beamforming and reconstruction methods such as delay-and-sum and backprojection can be employed to boost SNR and image quality.

## 2.3 Applications of Ultrasound Imaging

The following ultrasound imaging methods are some of the actively studied pre-clinical techniques to better understand, quantify and monitor tissue perfusion. These methods are not used in any experiments discussed in this thesis. Nonetheless, they are provided in more detail in order to draw a more accurate comparison between the experimental methods described in this thesis to other existing method.

### 2.3.1 Doppler Ultrasound Imaging

Doppler ultrasound imaging is based on the Doppler effect that states the acoustic wave generated at a specific frequency will be experienced differently by the receiver who may or may not be moving in relation to the acoustic source. The change in frequency, also known as the Doppler shift, is an important criteria used to determine the velocity of the moving observer or the source. For a single transducer both transmitting and receiving acoustic signals, the frequency received by the transducer will have changed by Doppler effect twice. The amount of shift,  $\Delta f$  is modeled by the expression,  $\frac{2f_0v \cos \theta}{c}$ , where  $\Delta f$  is the frequency shift,  $f_0$  is the transmission frequency by the transducer,  $f_r$  is the received frequency,  $c$  is the speed of sound and  $v$  is the velocity of the moving target. According to the expression, frequency shift is greater with increasing velocity and therefore, Doppler ultrasound imaging can be used to gain insight

about hemodynamic system as flow velocity in large vessels are much faster than movements in the surrounding tissue. As such, Doppler ultrasound technique was first applied for diagnostic purpose in estimating the blood flow velocity and the direction of the flow in the heart, which is known as Doppler echocardiography [17]. The frequency shift or motion-induced phase shifts are detected by the transducer is displayed on a color intensity map showing both the speed and the direction of the traveling particles superimposed on a ultrasound B-mode images to visualize flow and vascularity in context with surrounding tissue structure [18, 19, 20]. With pulse wave Doppler, the amount of frequency shift may cause aliasing if it is greater than the Nyquist frequency, which is half of the pulse repetition frequency (PRF) and is one of the main limiting factors on the performance of the system. As PRF is dependent on the imaging depth, the limitation on the maximum possible recording speed will increase as the distance between the transducer and the imaging sample decreases.

While color Doppler measures speed and direction at the location of the moving scatterers, it cannot detect flows in smaller vessels such as arterioles and venules due to low velocities in those vessels. Another type of pulse wave Doppler method known as Power Doppler imaging, on the other hand, is able to detect flows in smaller vessels due to its higher sensitivity. First reported by Rubin and Adler, power Doppler is based on the Doppler signal intensity from the scatterers rather than the frequency shift [21]. Therefore, it is independent of the sonication angle and it does not detect flow speed nor its direction. Because of its advantage as a high-sensitivity flow detection method, it may be used as a diagnostic tool in assisting biopsy and assessing ischemia due to rheumatoid arthritis and various types of cancer [22, 23, 24].

There also have been numerous attempt to establish power Doppler imaging as a perfusion estimation technique in small vessels even with its inability to explicitly estimate flow velocity. Dubiel et al. first proposed a semi-quantitative

way by estimating the mean power Doppler signal intensity within the region of interest in the organ [25]. This method, however, can only give relative estimation of perfusion as many factors, such as gain, attenuation and amount of RBCs in blood vessels, can modify or skew the obtained data. There is another method, published at a similar time, which is less dependent on the factors affecting the Doppler signal; it is known as a fractional moving blood volume (FMBV). FMBV is a method where the measured power Doppler signal is normalized in reference to a specific vessel with same imaging depth and condition that provides maximum power Doppler signal [26]. However, FMBV is not established as a clinical method for a couple of reasons. Power Doppler signals generated due to the tissue motion, known as a flash artifact, can attribute to a detection of higher-than-normal signal within the ROI and the most important limitation is that power Doppler images are exported to a photo editing software to choose a vessel of reference and obtain numerical values for pixel intensity normalized to such referenced vessel, which is time consuming and prone to operator related errors [27].

### 2.3.2 Contrast Enhanced Ultrasound Imaging

In previous sections, ultrasound imaging was based on the contrast between endogenous materials. However, contrast between structures can be increased by introducing an exogenous contrast agent into a specific type of tissue. Usage of contrast agents can greatly increase echogenicity of tissue that it binds to or blood as it is flowing in vessels, which results in visualization of small vessels that are resolvable but were difficult to identify due to low contrast. One of the more common example is in case of tumor vasculatures, which is marked by poorly defined and premature vascular networks with extremely slow flow speed ( $< 5\text{mm/s}$ ). Contrast enhancement technique arose when an improved US image quality was obtained after agitated saline was flowing through the

imaging site [28]. Since then, microbubbles of various sizes, which can be either filled with air, other type of gaseous materials or drugs have been introduced and approved by the food and drug administration (FDA) for clinical imaging and therapeutic use.

Using microbubbles can improve visualization of small vessels as they circulate, and it also means that perfusion rate can be indirectly estimated by measuring the amount of microbubbles flowing through vessels within a ROI. Most common way of detecting perfusion rate by bolus injection is to analyze the wash-in and wash-out dynamics during the circulation of microbubbles. The important measurable parameters that define the signal enhancement curve are time to peak, wash-in time wash-out time and mean transit time, where time to peak is the time it takes from zero intensity, which is just before the microbubbles start flowing into the ROI, to maximum intensity, wash-in time is the time from 5% intensity to 95% intensity, wash-out time is the time from peak intensity to zero intensity and mean transit time is the time that microbubbles pass through the ROI [29]. These parameters are found by fitting a mathematical model to the intensity curve and using the calculated parameters, the volumetric flow rate and the volume of blood can be calculated.

Circulating bolus allows volumetric flow rate to be estimated and insight to perfusion can also be gained when the bolus within the imaging area are destroyed by a short ultrasound pulse, also known as a destruction-reperfusion contrast enhanced ultrasound imaging. While gas-filled microbubbles are continuously delivered using infusion at a steady level, the bubbles within the ROI are destroyed using a high intensity ultrasound pulse, the flow is momentarily halted [29]. As the flow is resumed, the amount of microbubbles flowing back to the vessel within a region-of-interest can be measured. Because this method uses continuous infusion, the signal intensity from microbubbles reach

a plateau after initial wash-in. This can be modeled by a simple recovering exponential model, where the time constant can be a measure of reperfusion rate [29]. In comparison to the bolus injection method, infusion method is slightly more complicated due to extra system for maintaining the steady state of infusion throughout the experiment. Also, the hemodynamic status of a patient, properties and the location of the vessel of interest are determining factors choosing one method over others.

### 2.3.3 Strain Elastography

Since ultrasound imaging is able to visualize tissue structures through receiving echo signal, when mechanical changes, such as palpation and compression, are induced in the tissue they can be compared with the echo signals in the pre-induced state in order to determine displacement, elasticity and stiffness. The calculation and the mapping of elasticity or stiffness is called elastography. An important parameter associated with elasticity and stiffness is Young's modulus, which is defined by  $E = \frac{\sigma}{\epsilon}$  where  $\sigma$  is the induced stress and  $\epsilon$  is the resulting strain. To perform ultrasound elasticity imaging, displacement induced deformation on the sample must occur. One of the methods is by transmitting acoustic radiation force from a transducer to the imaging site [30]. Other methods involve displacement by compressive loading, which may be increased in small steps or have small, low-frequency perturbations (up to 10 Hz) after reaching maximum compression. Also, displacements can be either quasi-static where constant stress is applied or dynamic where the time-varying force is applied [31].

Elastic property of materials can be loosely categorized into three sets: linearly elastic, Cauchy elastic and viscoelastic. While linearly elastic materials have constant Young's modulus, Cauchy elastic materials have variable Young's modulus that is dependent on the applied strain and strain-rate. On the other

hand, viscoelastic materials exhibit strain- or strain-rate-dependent stress relaxation over time, which comes from a combination of viscous and elastic characteristic. Therefore, dynamic method is often preferred above the quasi-static method in materials that are heterogeneous and have exhibit either Cauchy elastic or viscoelastic properties as elastic moduli, such as Young's modulus, the shear modulus and the bulk modulus, would be dependent on the applied strain and strain-rate. On top of non-linear behaviors, materials may be anisotropic in nature, which means that a material have different mechanical properties depending on the direction of applied strain. One example of anisotropic and viscoelastic material is soft tissue; in addition to the complex material properties, the heterogeneity makes it extremely difficult to characterize the tissue *in vivo*.

One of the early breakthroughs in assessing elasticity using ultrasound was performed by Ophir et al. in determining axial displacement and strain from A-scans obtained from quasi-static compressions [32]. The methods in calculating strain have since then improved to encompass axial, lateral and elevational directions and many algorithms exist to boost efficiency and sensitivity. The algorithms can be categorized depending on whether or not it uses a phase information for estimation [33]. Displacement and strain estimation methods that require phase information include time-domain cross-correlation, phase-tracking and phase root tracking techniques while other methods, ones that do not require phase information, include power spectral methods, sum-amplitude, or sum-squared difference methods [33]. The estimation methods have also been improved through processes such as adaptive filtering of RF signals, displacement averaging or compounding, angular compounding of B-mode through beam steering and temporal stretching of signal from the deformed state, which increase sensitivity and reduce noise [33].

## 2.4 Photoacoustic Effect

The photoacoustic effect, discovered by Alexander Graham Bell in 1880, is based on the phenomenon where the optical absorber, also known as a chromophore, after being illuminated, releases acoustic energy as it cools. The generated acoustic signal can be detected by an acoustic receiver. In summary, a chromophore must undergo three events, as shown in figure 2.1, in order for the photoacoustic effect to occur: 1. absorption of light, 2. conversion of optical energy to heat, which creates temperature rise and 3. the thermoelastic expansion, which in turn allows for the emission of acoustic wave. For an optimal signal generation the laser pulse must be shorter than both thermal and stress confinement times, which are respectively defined as  $\tau_{th} = \frac{d_c^2}{4D_T}$  and,  $\tau_{st} = \frac{d_c}{v_s}$ , where  $d_c$  is the spatial resolution,  $D_T$  is the thermal diffusivity and  $v_s$  is the speed of sound [34]. For medical ultrasound, the pulse duration must be less than 100 ns [35]. Once both relaxation time criteria are met, the volume expanded by the laser pulse can be modeled as  $\frac{dV}{V} = -\kappa p(\vec{r}) + \beta T(\vec{r})$ , where  $\kappa$  is the isothermal compressibility,  $\beta$  is the thermal coefficient of volume expansion,  $p(\vec{r})$  is change in pressure and the  $T(\vec{r})$  is the change in temperature [36]. Therefore, the initial photoacoustic pressure can be defined as  $p_0(\vec{r}) = \frac{\beta T(\vec{r})}{\kappa}$ , and  $T = \frac{A_e}{\rho C_v} = \frac{\mu_a F(\vec{r})}{\rho C_v}$ , where  $\rho$  is the mass density,  $C_v$  is the specific heat capacity at constant volume,  $\mu_a$  is the absorption coefficient,  $F(\vec{r})$  is the local fluence and  $A_e$  is the absorbed energy density [34, 36]. The initial photoacoustic pressure can also be written in an alternative form,  $p_0(\vec{r}) = \Gamma \mu_a F(\vec{r})$ , where  $\Gamma$  is the Gruneisen parameter, which increases as the temperature increases [36]. For the purpose of applying photoacoustic imaging *in vivo*, the temperature rise due to laser pulse must be kept to a minimum, which then, the Gruneisen parameter can be treated as a constant.

In clinical settings, nearly every tissue cell that make up the body can be

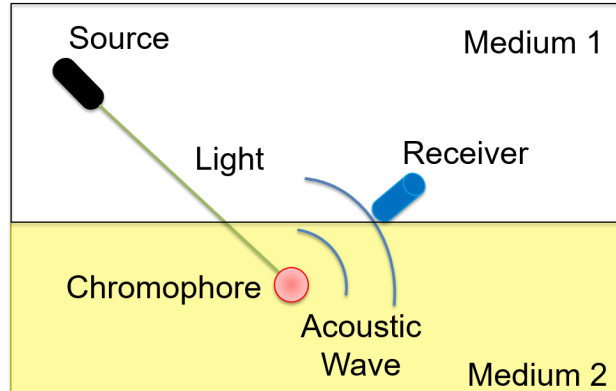


FIGURE 2.1: A basic schematic of photoacoustic effect. In a clinical setting, medium 1 is often ultrasonic gel or water and medium 2 is soft tissue

considered as chromophores that are prone to photoacoustic effect with illumination and different type of chromophores, such as melanin, proteins, DNA, RNA, muscle, lipids, hemoglobin and water all have their own characteristic absorption spectrum. Therefore, photoacoustic imaging is highly dependent on, not just the pulse intensity, but also the frequency content of light pulse in order to filter and obtain necessary data from imaging. It is especially critical to avoid wavelengths that can cause water to emit strong photoacoustic signal as it is present in large proportion throughout the body. Hemoglobin, however, has a characteristic absorption spectrum somewhere in the visible and near-infrared wavelength ranges. At this range, hemoglobin is more optically absorbing than water, which allows them to be detected at higher acoustic signal than water.

## 2.5 Photoacoustic Imaging

Photoacoustic imaging, as a clinical tool, has gained momentum in the last half-century with the development of laser in 1960, allowing high power light source to become more readily available [37]. This allowed light pulse to achieve

deeper penetration and deliver more power in a shorter amount of time, allowing emission of ultrasound from chromophores with improved SNR. The setup for photoacoustic imaging resembles very closely to that of ultrasound imaging as both modalities must be able to receive ultrasound signal. Photoacoustic imaging (PAI), however, replaces an acoustic source with an optical source. Depending on the system setup, PAI can be categorized into two types: reflection mode Photoacoustic Microscopy (PAM) and transmission mode PAM. The most basic setup would be the transmission mode PAM as the source and the receiver are not integrated. Irrespective of imaging modes, transmission PAM would be that the sample must be thin in order to have uniform fluence as optical source is located opposite to the acoustic receiver. For thicker samples, the optical source may have to be at an angle, which may cause non-uniform fluence and larger scattering. These imaging types can be sub-divided into optical-resolution PAM (OR-PAM) and acoustic-resolution PAM (AR-PAM). These categorization comes from how lateral resolutions are determined. With the OR-PAM, greater optical focus than acoustical focus results in optical focus to determine the lateral resolution while the AR-PAM, the situation is reversed. Often, resolution of OR-PAM is limited by the diffusion limit, which is  $\sim 1$  mm in tissues. In contrast, AR-PAM can achieve spatial resolution that exceeds optical diffraction limit because the acoustic wave is less scattering in tissue. The imaging depth of an AR-PAM can reach diffusive regime where the amount of optical energy scattering back to the receiver from that regime is minimal while the acoustic energy generated by tissues in diffusive regime may be non-trivial.

Being able to detect photoacoustic signal from blood allows the label-free assessment of hemodynamic status and vascularity non-invasively. Additionally, using a high-frequency transducer ( $> 20$  MHz) improves resolution, which can allow visualization of small networks such as arterioles and venules at deeper locations than pure optical or acoustical imaging methods. It may also be

able to detect photoacoustic signals from capillaries, albeit too small to be resolved spatially. Being able to see small vascular networks are crucial in monitoring vascular health, which can be used to understand tissue hypoxia and unrestricted angiogenesis due to tumor growth and ischemia due to pressure and diabetic ulcers. Using photoacoustic imaging, there is a potential for detecting ischemia early before it leads to more extreme conditions such as limb necrosis, which could reduce cost involved in surgery and treatments.

Because photoacoustic imaging transmits optically and receives acoustically, both characteristics can be exploited to estimate blood flow in small vessels. When a ultrasound transducer receives a photoacoustic signal generated from a moving source, the frequency of the signal is shifted due to the Doppler effect and the calculated frequency shift can be used to quantify blood flow in small vessels label-free, which is known as the photoacoustic Doppler imaging [38]. Another type of photoacoustic flow imaging, done by Brunker and Beard, calculated flow by cross-correlation of photoacoustic signals obtained from two laser pulses with a small, and known time delay [39, 40]. While both methods have shown to detect speed as low as  $\sim 5\text{mm/s}$ , they have suffered from shallow penetration depth and poor axial resolution.

Photacoustic imaging, when combined with various ultrasound imaging techniques, is able to provide data that complements the one obtained by other imaging systems. For example, combination of photoacoustic imaging with regular B-mode ultrasound imaging is able to contextualize vascularity to surrounding tissue structures, and combining photoacoustic imaging with color Doppler imaging can allow detection blood flow with directionality.

### 2.5.1 Functional Photoacoustic Imaging

Due to different types of chromophores having their own respective absorption spectrum, photoacoustic imaging can reveal vastly different information depending on the wavelength content of the laser source. However, using a single wavelength may not necessarily uncover all the information regarding absorption and scattering properties of chromophores. Such problems can be overcome by performing photoacoustic imaging with cycling multiple wavelengths. One of the prime examples of multi-wavelength photoacoustic imaging is to estimate oxygen saturation in vessels. This is because multi-wavelength photoacoustic imaging is able to extract absorption coefficient of oxy- and deoxy-hemoglobin. However, current methods in calculating oxygen saturations are often noisy and are unreliable as Gruneisen parameter is treated as a constant whereas it is variable depending on the material property and more importantly, the initial fluence from the source, regardless of the wavelength, are considered equal. Irrespective of the unreliability, changes in the oxygen saturation relative to a known level can be performed, which can be calibrated using pulse oximeter or oxygen saturation catheter. Such techniques have been implemented in measuring oxygen saturation of vessels in cerebral circulations, internal organs such as gastrointestinal tract and lymphatic system [41, 42]. Depending on the choice of wavelengths, potential applications also includes imaging melanoma and angiogenesis [43].

## 2.6 Other Pre-clinical and Clinical Perfusion Imaging Systems

Techniques to image and characterize the microvasculature have seen recent developments. Currently, there are various optical and non-optical based microvascular imaging system with their own advantage and disadvantages compared to PA imaging. Major ones include Laser Doppler perfusion imaging (LDPI), laser speckle contrast imaging (LSCI), and thermal imaging to name a few, and non optical-based imaging includes dynamic contrast-enhanced magnetic resonance imaging (DCE-MRI) and computed tomography (DCE-CT) and positron emission tomography (PET) to name a few [44]. The methods and its limitations of the imaging methods are discussed in more detail.

### 2.6.1 MRI

With the assistance of exogenous contrast agents, MRI can be used to estimate perfusion by comparing the baseline image with the contrast enhanced images as bolus perfuses to tissues. When MRI is performed with the presence of contrast agents, it affects relaxation time of polar molecules, known as  $T_1$  and  $T_2$ , where the first term and second term determines the reduction in signal intensity and the degree of signal broadening respectively [45]. Due to the choice of contrast agents that may affect one relaxation time more dominantly than the other, MRI perfusion imaging techniques are divided into two types: dynamic susceptibility contrast enhanced (DSC) MRI and dynamic contrast enhanced (DCE) MRI [45]. While perfusion MRI has been used clinically for many decades, the system is bulky and expensive to run. So while it is an established clinical technique, it is less available compared to other imaging techniques such as ultrasound and CT.

### 2.6.2 Computed Tomography

Computed tomography scans uses X-ray to determine how well blood perfuses to tissues. It is used to determine perfusion in either the brain, the heart or the liver. Perfusion computed tomography is fast and painless but it requires an delivery of iodinated contrast agents to an organ being imaged. In the brain, computed tomography measures cerebral blood flow, cerebral blood volume and mean transit time that is defined as the average transit time of blood through a region of interest [11]. It is used to hemodynamic status associated with brain such as brain ischemia, infarct and penumbra [46]. In comparison to non-enhanced computed tomography, perfusion computed tomography requires additional dose of radiation, and image acquisition time takes longer[47].

### 2.6.3 Positron Emission Tomography

Positron emission tomography is performed by detecting a pair of gamma rays emitted by radionuclide, which is either injected, inhaled or swallowed [10]. It is used in measuring myocardial perfusion and takes anywhere from 4 to 20 minutes depending on the radionuclide, which are most often a bolus containing  $^{13}\text{N}$ -ammonia or  $^{82}\text{Rb}$ -Rubidium [48]. The total time for image acquisition, including the time the bolus travels to the imaging site, takes about 10 minutes at minimum [48]. Therefore, positron emission tomography cannot be used for real-time monitoring of perfusion not just due to the length of time but also because of the amount of radiation exposure if it was to be used for monitoring.

### 2.6.4 Laser Speckle Imaging

Laser speckle perfusion imaging is used commercially as a perfusion rate estimation technique, which is based on the speckle pattern generated by illuminating a light of within visible spectrum on a tissue layer. The idea of Laser speckle

imaging techniques revolves around the de-correlation of speckle patterns spatially or/and temporally to determine the perfusion rate [49]. The laser speckle perfusion imaging is based on combining laser speckle contrast analysis and laser speckle imaging, which are based on spatial and temporal de-correlation respectively [49]. This technique is considered 2D as all of the depth information is lost when determining the perfusion rate, which means that the measured flow rate includes the rates in larger vessels such as arterioles and venules that will create a systematic bias in perfusion rate measurements in the microvessels [50].

### 2.6.5 Nailfold Capillaroscopy

Nailfold capillaroscopy is a technique designed to view the capillaries in the nail-bed in order to assess microvascular health related rheumatism, sclerosis and Raynaud's syndrome [51]. The method is straightforward as the nailfold, on which the drop of immersion oil is applied for enhanced transparency, are viewed under optical devices such as stereomicroscope or digital videocapillaroscope designed specifically for the task [52]. However, it suffers from low reproducibility with the use of stereomicroscope and requirement of high precision when using videocapillaroscopy [52].

### 2.6.6 Near-Infrared Spectroscopy

Near-infrared spectroscopy has been used in clinics as a way to monitor the oxygen saturation and perfusion. The technique is based on interrogating the tissue layer, which is heterogeneous with many optical scatterers and absorbers, with multiple wavelength within the near-infrared spectrum. Because the detection is based on the amount of light returning back to the imaging probe, the entrance of ambient light has to be minimized [53]. With NIRS, the transmission of up to  $1.95 \text{ J/cm}^2$  at the depth of 30 mm has been achieved with less than 2 degree Celsius increase in the local skin temperature [54].

### 2.6.7 Reflectance Spectroscopy

Reflectance Spectroscopy is based on the elastic scattering of transmitted light that returns to the location of the source, which will also have the ability to receive light [55]. Elastic scattering is defined as scattering of light without the change in wavelength. This creates back-scattering or a scattering event which allows certain percentage of light to be scattered directly back to the source-receiver. The percentage of power being received will vary depending on the wavelength as molar extinction coefficient of different materials in the tissue are wavelength-dependent.

## 2.7 Deformation of Vessels Due to External Load

Systolic and diastolic blood pressure of a human is a well understood subject as sphygmomanometer has been used for more than a century in the estimation of the arterial pressure. However, sphygmomanometer cannot be used to measure blood pressure in venous circulation or smaller vessels in arterial circulation since the measurement technique depends on the detection of pulsatile flow. Also, sphygmomanometer does not monitor vessel behaviors as pressure cuff is inflated and deflated, which could be an essential quality to reduce errors in pressure estimations. One of the tasks in understanding vessel behavior is to estimate displacement of a vessel wall during external compression. Early works involved buckling of a thin circular cylindrical tube or a ring due to a uniform external load and understand how the shape is altered [56]. More specifically, induced changes in the normalized area of the cylinder due to the change in the transmural pressure,  $p_t$ , which is the difference between the internal pressure and the external pressure, has been plotted, as shown in figure 2.2 [6]. The variable  $p$  on the top left of the figure 2.2 is denoted as  $p_i$  in this thesis. Shapiro

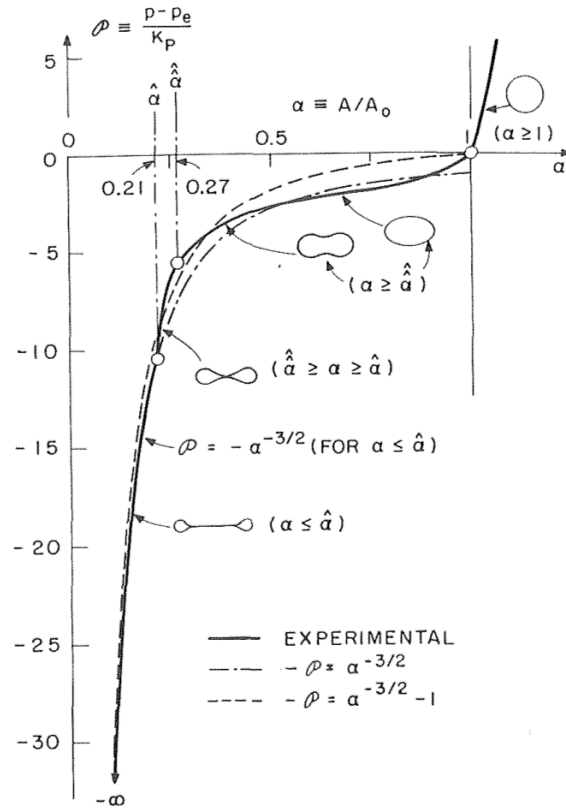


FIGURE 2.2: Changes in the Normalized Area and the Shape of a Vessel with Changes in the Transmural Pressure [6]

et al. have also come up with the mathematical model attempting to explain such behavior:

$$-\frac{p_t}{\kappa_p} = -\left(\frac{p_i - p_o}{\kappa_p}\right) = \alpha^{-n} = \left(\frac{A}{A_0}\right)^{-n} \quad (2.1)$$

where  $p_i$  is the internal pressure,  $p_o$  is the external pressure,  $\kappa_p$  is the parameter proportional to the bending stiffness of the tube wall,  $\alpha$  is the dimensionless normalized cross-sectional area of the tube,  $A$  is the current cross-sectional area and  $A_0$  is the undeformed cross-sectional area. This model has not been studied in either *in vivo* experiments nor in a phantom study and therefore, the extent of its applicability is unknown. In this thesis, we investigate the applicability

of this model to *in vivo* experiments and propose new models which are aimed at facilitating vascular pressure estimation from compression experiments.



## Chapter 3

# Relative Microvascular Pressure Sensing

This manuscript has been published as M. Choi, R. Zemp. "Relative Microvascular Pressure Sensing" Proc. SPIE 9708, Photons Plus Ultrasound: Imaging and Sensing 2016; 97081D (2016); doi: 10.1117/12.2213607. Some of the contents have been modified for the thesis.

### Abstract

Microcirculation may be characterized by the vascular pressure as it is influenced by pressure-driven perfusion. Cross-sections of blood vessels can be visualized by photoacoustic imaging and compressing on vessels causes deformation. The photoacoustic signals of blood, when compressed to the point of vessel collapse, may or may not vanish depending on the buckling process it undergoes due to viscoelastic relaxation of soft tissues. The measured external pressure required to compress vessels are many times higher than ordinary physiological values and are inaccurate because it is not equal to the amount of pressure at the outer boundary of each vessel nor the relationships between them are known. Therefore, the blood pressure inside various vessels of interest are ranked relative

to each other instead of denoting them with measured pressure values and up to four vessels have been simultaneously tracked and ranked. Also, to minimize the number of compression required to obtain pressure values for a set of vessels, a capacitive force sensor is used and the image and force measurement are synchronized.

### 3.1 Introduction

Microcirculation is an important aspect when considering health as microvasculature provides exchange of materials in tissues. Interruption of microcirculation can create ischemic ulcers which can result in cell necrosis and amputation may have to be performed [57]. Therefore, restoring and maintaining normal vascular function is essential for patients suffering not just from ischemic ulcers but also suffering from septic-shock, diabetes, hypertension and etc [58, 59, 60, 61]. In addition, microcirculation can be impacted by angiogenesis as the flow of blood in small vessels are influenced by pressure-driven perfusion and hence knowing the blood pressure in small vessels are extremely important [62]. However, current techniques to measure blood pressure non-invasively are often limited to large arteries using sphygmomanometer and measuring blood pressure in smaller arteries require invasive catheters.

To measure the blood pressure of small vasculatures, photoacoustic imaging can be employed as hemoglobin are chromophores. Therefore, at sites where there is no blood flowing, there should not be any photoacoustic signal generated. Using these ideas, physical manipulation of small vessels underneath the skin surface can be visualized using by PA imaging where the photoacoustic signal vanishes when the vessel compresses fully under external pressure. From Han et al, small vessels will collapse when the transmural pressure, which is the difference between the internal and the external pressure) reaches a certain critical value below zero [63]. This paper attempts to validate the possibility

of correlating the blood pressure with the external pressure through the use of photoacoustic and ultrasound imaging for phantom experiments and to further deduce the internal pressure of the microvasculatures through *in vivo* experiments.

## 3.2 Phantom Experiment

### 3.2.1 Experimental Setup

For the purpose of validation, a microcellulose tube (the diameter of 200  $\mu\text{m}$  and the wall thickness of 7  $\mu\text{m}$ ), is inserted through the phantom, where one end is threaded into the syringe needle, and the other end is left open to let the blood exit. Additionally, two types of phantoms are prepared: 10% m/V gelatin and the chicken breast tissue. With this setup, sheep blood is flowed through the tube with the flow rate set using a syringe pump. The flow is visualized using the imaging apparatus described below and the flow will be stopped by compressing on the surface of the phantom. Also, the compression force will be measured by placing the scale below the phantom. The imaging apparatus includes VEVO 2100 and VEVO LAZR from Visualsonics (Fujifilm Inc.), which can perform ultrasound and photoacoustic imaging simultaneously and in real-time. The imaging is done using LZ 550 transducer which has a transmit frequency of 40 MHz, receive bandwidth of 32 – 55 MHz, and maximum width and depth of 14.08 mm and 15 mm respectively.

### 3.2.2 Results and Limitations

Even when transmural pressure becomes less than zero, the tube may or may not close fully, which can be visualized with the imaging system, and some signals may remain regardless of the pressure being applied. These cases may be due to the way the tubes buckle under external pressure. The transducer

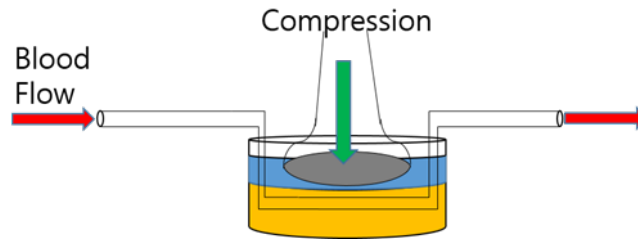


FIGURE 3.1: A basic schematic of the compression experiment. The transducer surface (gray) compresses on the phantom (yellow) surface directly. The phantom is submerged in water (blue) to provide impedance matching. A scale (not shown) is placed below the phantom to measure the applied pressure.

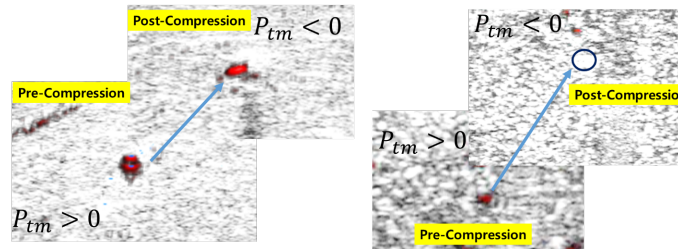


FIGURE 3.2: Case 1 (left): The vessel compresses and the top and the bottom of the vessel can no longer be differentiated, however, the signal does not vanish even when the load double after signal merges. Case 2 (right): The vessel completely vanishes after the transmural pressure reaches a critical value. The flow stoppage is visualized for both cases.

used to compress on the surface is covered by a concave shell, which allows the edges to be pressed prior to the center, and this may cause the pinching of the tube to occur at places away from the imaging plane. Therefore, multiple criteria must be established to determine the exact time of collapse.

The gelatin phantom was prone to chipping under external compression and no plausible data could be obtained due to the fact the tube buckled laterally instead of compressing to closure. However, the chicken tissue was able to hold better under such pressure up to the point where the tube closed. With each flow rate, which corresponds to the internal pressure, the transducer was

compressed with the same tube and without changing the location of the tube within the phantom. The flow rate was set from 0.1 ml/min to 0.25 ml/min in 0.05 increments, which converts to the expected velocity of 5.5 cm/s to 13.7 cm/s. The relationship between the external compression at which flow stops and the internal pressure is shown in figure 3. After the first set of compressions were performed, the flow rate was reduced to 0.1 ml/min again and the experiment was repeated. As shown, the second set of experiments had much higher values compared to the first set, due to chicken breast tissues, under external compression, being influenced by viscoelastic relaxation, which is both nonlinear and time-dependent. Also, the nature of the phantom resulted in irreversible deformation changes on tissues after prolonged experimentation times. To better understand the tissue behavior under external loading, various imaging techniques, such as supersonic shear imaging, strain imaging and etc., can be used to estimate the tissue stiffness which can aid in determining the required external pressure more accurately. Also, irreversible deformation will not be a problem when performing *in vivo* experiments as the blood continuously perfuse to recover from deformation. Since the compression measurement is possible on phantoms, *in vivo* experiment is performed to further validate the technique.

### 3.3 In Vivo Experiment

#### 3.3.1 Experimental Setup

The vessel detection setup remains identical to the phantom experiment setup. However, phantoms will be replaced by a human arm or a human hand, which is submerged in water. Unlike, the phantom experiment, a small piece of ultrasound gel pad is inserted into the transducer shell, which has concave edges, in order to improve the delivery of external pressure to vessels deep within tissue surface. Since scale cannot log data, multiple compressions are done in order

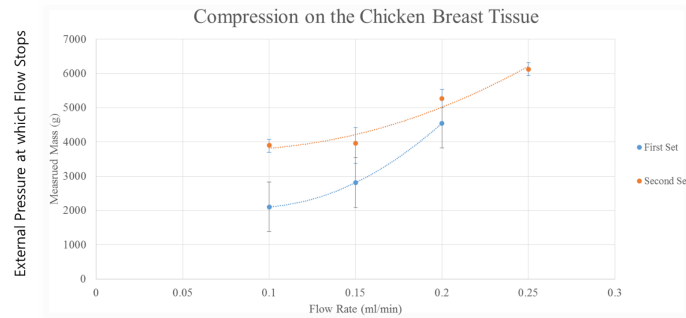


FIGURE 3.3: Compression of the transducer on the thin chicken breast tissue. The flow rate corresponds to the internal pressure which is set by the syringe pump and the measured mass is the value shown on the scale at which the vessels close. The measured mass corresponds to the external pressure.

to find the required external pressure for vessels of interest. The image frames, once saved, will be used to perform vessel tracking, which is used to rank the relative pressure of the vessels of interest.

To minimize the compression even more, another experiment is done where a capacitive force sensor, from LoadStar Sensors, is attached above the transducer to in order to determine the amount of applied force in real-time. The sensor can be synchronized with the imaging system using a DAQ board which starts logging data from the sensor after it has been triggered by the imaging system. However, this system will be implemented with the vessel tracking algorithm in the future.

### 3.3.2 Vessel Tracking Algorithm

Once the image sequence is obtained, it is run through MATLAB where the ultrasound the photoacoustic image data are split. The thresholding and filtering of the photoacoustic image is done and is followed by centroid detection algorithm. With the centroid of the vessels of interest found, small regions of interest, slightly larger than the vessel are created. Then the successive frame

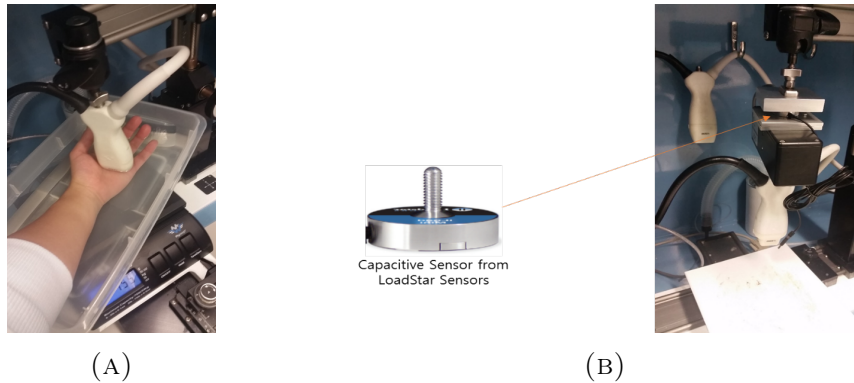


FIGURE 3.4: (a): The *in vivo* experimental setup. (b): The capacitive sensor can measure both compression and tension. When the transducer is hanging in mid-air, the sensor is being pulled down, which will be considered as the zero point (tare value).

is uploaded and is overlaid with the regions of interest drawn in the previous frame. The movement of the centroids are detected and the regions of interest move according to the centroid movement until the vessel signals vanish. After the entire image sequence is run through, the frame at which the vessel signal disappeared is denoted on the first frame, showing the relative pressure distribution in the microvasculature.

### 3.3.3 Results and Discussions

The synchronization of the sensor signal and the image are shown below <sup>1</sup>. The change from scale to the force sensor greatly increased the accuracy of the measurement where reflex motions influences the pressure being measured on the scale. However, it is known that, as transducer pushes down, the effect changes with every compression due to viscoelasticity of soft tissues. The degree of viscoelasticity is different for various parts of the body and the effect of

<sup>1</sup>The videos can be found on the SPIE publications website: <https://www.spiedigitallibrary.org/conference-proceedings-of-spie/9708/1/Relative-microvascular-pressure-sensing/10.1117/12.2213607.full>

viscoelasticity can vary with duration and the amount of stress applied on the tissue[64]. Therefore, the amount and the time of compression must be kept minimal. In addition, with the use of the sensor, the number of compression required decreases as the applied pressure, which can increase nonlinearly, can be detected. The pressure measured, when converted is greater than the physiological blood pressure ( $>120$  mmHg). Therefore, the plot is normalized to the maximum value of 100 mmHg, where it is assumed that the blood pressure at small vessels are slightly lower than at large major arteries.

The ranking of pressure inside small vessels are relative and the actual internal blood pressure is unknown, however, the algorithm was able to track and rank the relative pressure of four vessels at the same time. The actual pressure being applied at the vessel is unknown due to the viscoelastic relaxation. Again, the compression itself has to be kept relatively short in order to minimize relaxation effect. Also, the deformations due to compression, unlike phantom experiments, are reversible depending on the magnitude and the duration of the compression. The algorithm is currently limited to tracking vessels where there is no significant artifact and to track until the signal disappears. Because the cross-sectional area of the vessel forms a hysteresis with the change of external pressure, the algorithm cannot track the vessel when it reappears.

### **3.3.4 Conclusion**

We have been able to show the behavior of blood vessels under external compression and non-invasively, using commercially available photoacoustic and ultrasound imaging system. The relative magnitude of pressure within small blood vessels can be denoted using the developed color coding algorithm according to their time of disappearance. The future work will involve unifying the synchronization of imaging-force detection system and the color coding algorithm. In addition, better estimation of viscoelastic behavior and the critical

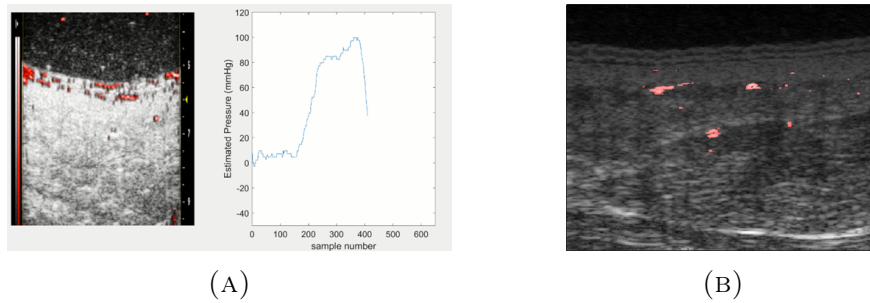


FIGURE 3.5: (A) The synchronization between imaging and the force sensing. (B) The tracking and color coding of four vessels, three vessels disappear at similar time and the coded colors are similar. The vessels are detected only up to where the signals disappear

transmural pressure will allow us for pressure measurement of higher accuracy. Lastly, blood pressure measurement of small arteries using compression technique is sought as a method to calibrate the blood pressure of other small vessels and determine their absolute pressure.



## Chapter 4

# Compression-tracking photoacoustic perfusion and microvascular pressure measurements

### Abstract

We propose a method to measure blood pressure of small vessels non-invasively and in-vivo: by combining PA imaging with compression US. Using this method, we have shown pressure-lumen area tracking, as well as estimation of the internal vessel pressure, located 2 mm deep in tissue. Additionally, re-perfusion can be tracked by measuring the total PA signal within a region of interest (ROI) after compression has been released. The ROI is updated using cross-correlation based displacement tracking<sup>1</sup>. The change in subcutaneous perfusion rates can be seen when the temperature of the hand of a human subject drops below the normal.

### 4.1 Introduction

Hemodynamic properties of vessels in peripheral circulation such as perfusion rate, lumen characteristics, and pulsatility of flow are important criteria in

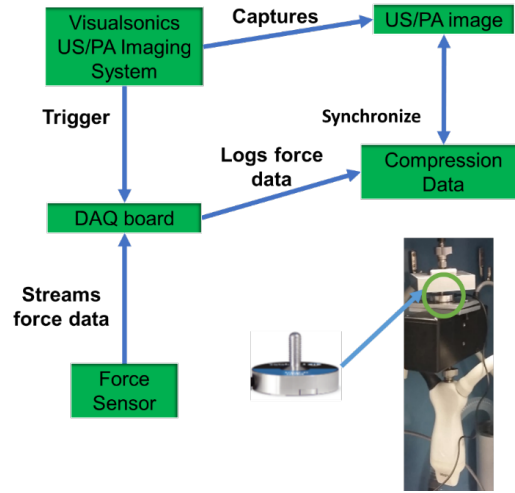


FIGURE 4.1: Schematic of Force Detection and US-PA Dual Imaging

diagnosing vascular disease. These properties are related to the blood pressure within those vessels and the buckling pressure of the lumen walls. Currently, however, there is no method to assess blood pressure in small vessels.

We propose a method to measure blood pressure of small vessels non-invasively and *in-vivo*: by combining PA imaging with compression US. Using this method, we attempt to track the changes in lumen area with increasing applied external pressure. By fitting a curve to the pressure-area data, we estimate the internal vessel pressure, located at depth of  $>1$  mm in tissue. Additionally, re-perfusion can be tracked by measuring the total PA signal within a region of interest (ROI) after compression has been released. The ROI is updated using cross-correlation based displacement tracking by Rivaz et al.[65]. We attempt to detect the changes in perfusion rate when the hand of a human subject has been submerged in an ice-bath for up to 2 minutes.

## 4.2 Methods

A preclinical US and PA dual imaging system VEVO 2100 is used to record both US and PA images in real-time and the force sensor is used to continuously track the applied force. Once the imaging starts, it triggers DAQ board to initiate logging the force data, which will be synchronized with each frame.

## 4.3 Microvascular Pressure Measurement

The relationship between the area of blood vessels and the external pressure is experimentally constructed by Shapiro[6]. This equation is modified to account for the pressure being absorbed before by the layer of soft tissues. The original equation by Shapiro is shown below:

$$-\left(\frac{p_i - p_e}{\kappa_p}\right) \propto \left(\frac{A}{A_0}\right)^{-n} \quad (4.1)$$

Where,  $p_i$  is blood pressure of the vessel,  $p_e$  is external pressure applied to the vessel,  $\kappa_p$  is critical pressure of vessel collapse,  $A$  is current cross-sectional lumen area,  $A_0$  is cross-sectional lumen area in the unstressed state and  $n$  is size reduction constant, known to be  $\frac{3}{2}$  for veins<sup>2</sup>.

Our strategy for measuring intravascular pressure is to (1) apply an external force to compresses the tissue using the photoacoustic transducer head. (2) Track vessels using centroids of photoacoustic vessels signatures. (3) Track the effective vessel area (from the photoacoustic data) as a function of applied compression. (4) Use measured forces to estimated applied pressures around vessels in deep tissues using finite element models, comparing with strain imaging maps (data not shown). (5) Fit the vessel-area versus external pressure data to the above pressure-area equation to extract fitting parameters of vessel compliance and internal pressures. Fig. 4.2 shows ultrasound-photoacoustic images of the vessel collapse process. Fig. 4.3 shows the fitted pressure-area curves, while

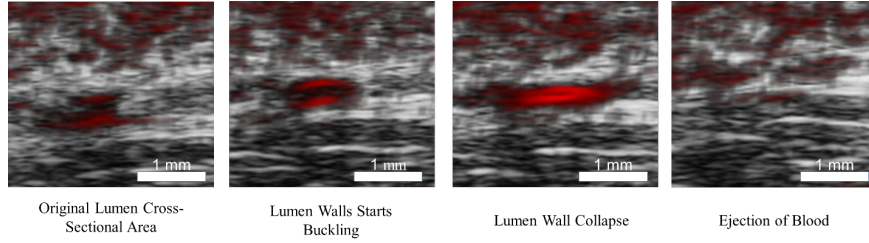


FIGURE 4.2: Different Stages of Vessel Buckling Due to Increasing External Pressure

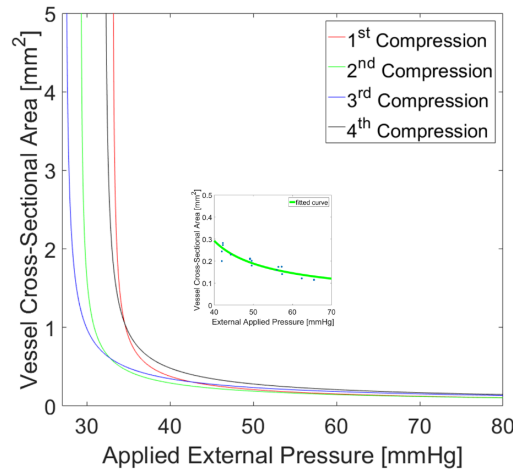


FIGURE 4.3: (Large) Fit of Multiple Pressure-Area Curve for a Single Venule. (Small) Zoomed in Data Fit of Second Compression.

the fitting results are illustrated in Table 4.1. In doing the fitting, we assumed  $n = \frac{3}{2}$ , and  $A_0 \approx A_{uncompressed} = 0.385 \text{ mm}^2$  (From US Image).

## 4.4 Compression-Reperfusion Rate Estimation

In addition to estimation of microvascular pressure and compliance, we propose a method for estimating perfusion. In particular, we apply compression to tissues to exclude blood and then use photoacoustic imaging to image the reperfusion process and fit the net photoacoustic signal in a region of interest to

	$\kappa_p$ (mmHg)	$P_i$ (mmHg)
1 <sup>st</sup> Compression	6.783	33.02
2 <sup>nd</sup> Compression	7.175	29.16
3 <sup>rd</sup> Compression	10.82	27.33
4 <sup>th</sup> Compression	11.14	32.06

TABLE 4.1: Estimated Kappa and Internal Pressure of a Single Venule

a recovering exponential model to extract reperfusion time-constants. We design a simple experiment to validate measured differences in reperfusion time in various cold-exposures. Longer cold-exposure in an ice-bath is known to reduce perfusion rates. This is observable by depressing one's fingernail and noting the time to recover from a white- to a pink-color. The proposed photoacoustic compression technique may enable similar measures but in deep tissue and may be applicable to numerous clinical problems such as evaluating perfusion in bed sores, diabetic ulcers and pre-ulcers, and in tumors.

Re-perfusion time can be estimated by fitting the data to a solution to the first-order ODE given below:

$$PA(t) = (PA_{max} - PA_{min}) (1 - e^{-t/\tau_c}) + PA_{min} \quad (4.2)$$

Where  $PA(t)$  is the PA signal at time  $t$ ,  $PA_{max}$  is signal before compression,  $PA_{min}$  is signal during maximum compression and  $\tau_c$  is the perfusion time constant.

Fig. 4.4 shows a fit of this model to recovering photacoustic mean signals

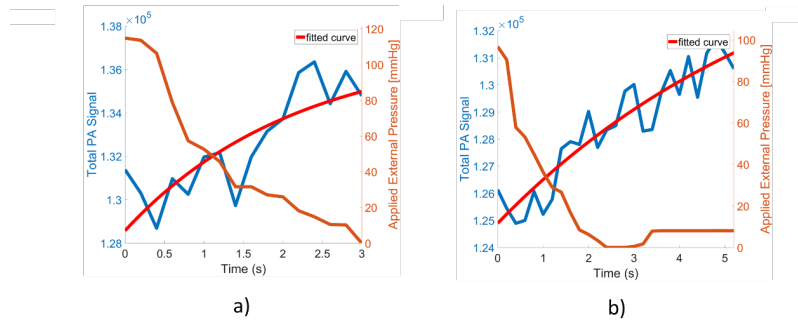


FIGURE 4.4: Change in Total PA Signal with Applied External Pressure on a Forearm Submerged in an ice-bath and the Curve Fitted to the Total PA Signal According to the Equation shown above a) 1 min. in an ice-bath b) 2 min. in an ice-bath

after a compression event. The reperfusion times are 2.16s and 6.76s for 1 min and 2 min cold-exposures, respectively.

## 4.5 Conclusion

We have demonstrated a novel approach to quantitative photoacoustic-compression-based measurements of intravascular pressure and reperfusion rates. The methods introduced may prove valuable for assessing perfusion and pressure in a variety of clinical situations where there are currently no known methods for non-invasive assessments of these parameters.

## Acknowledgement

We gratefully acknowledge funding from a Prostate Cancer Canada Movember Discovery Grant, NSERC, CIHR, the Canadian Cancer Society, and the Canada Foundation for Innovation, Leaders Opportunity Fund.

## Chapter 5

# Perfusion Rates Tracking

### Abstract

Tissue perfusion is essential for transporting blood-oxygen and nutrients. Measurement of tissue perfusion rate would have a significant impact in clinical and pre-clinical arenas. However, there are few techniques to image this important parameter and they typically require contrast agents. A new label-free methodology based on tissue compression and imaging with a high frequency photoacoustic-ultrasound system is introduced for estimating and visualizing tissue perfusion rates. Experiments demonstrate statistically significant differences in depth resolved perfusion rates in a human subject with various temperature exposure conditions.

### 5.1 Introduction

Tissue perfusion can be compromised in a number of disease conditions, including peripheral vascular disease (PVD), sepsis and septic shock, diabetic ulcers, pressure ulcers, and cancer among others [66, 67, 68, 69]. Being able to measure tissue perfusion rates could prove highly impactful to clinical practice. However, few methods exist for doing so. One method for rough assessment of whole limb perfusion is assessment of cutaneous capillary refill time (CRT), which is done by pressing on a nail-bed or a finger for five seconds and measuring the time for

the pink color to return. However, CRT is devoid of metrics for diagnostic comparisons and is highly variable depending on the patient's size, weight, tissue composition and much more [70, 71, 72, 73]. Therefore, it is used to roughly gauge perfusion abnormality due to hypothermia, PVD, dehydration and shock. It is not an imaging technique and provides no spatially-resolved information about tissue perfusion.

Laser Doppler speckle (LDS) imaging (e.g. PeriMed), along with other speckle based imaging such as laser speckle contrast imaging are examples of commercial perfusion-rate tracking system on a peripheral vascular system [49]. However, these systems only measure very superficial blood-flow changes, are not fully quantitative, and provide no depth-resolution [74, 75].

Depth-resolved perfusion imaging methods in peripheral vascular system used for preclinical purposes typically require contrast agents and thus limit applicability to screening tasks [76]. Ultrasound imaging is able to measure the rate of perfusion by injecting microbubble contrast agents and destroying them at the imaging site. The reperfusion of these contrast agents is observed and signals are fit to models in order to estimate spatially-resolved reperfusion times [77, 78, 79]. While the destruction-reperfusion ultrasound imaging technique is a powerful means of imaging tissue perfusion, some work has shown that the destruction of microbubbles may damage microvascular walls [80, 81].

Other preclinical methods of measuring perfusion rates such as Dynamic Contrast-Enhanced MRI also typically require contrast agents and are not sufficiently low cost or high throughput for widespread screening tasks. These applications have been applied to cerebral perfusion, myocardial perfusion, and cancer imaging, among others [82, 83].

Tissue perfusion has previously been defined as the volume-flow rate of blood exchange per given mass of tissue. In this study we use a technique similar to ultrasound destruction-reperfusion imaging to estimate the so-called "re-fill

---

rate” associated tissue reperfusion. In the contrast-enhanced ultrasound approach, microbubble contrast agents are injected intravenously and those passing through the imaging plane are subsequently destroyed using an intense ultrasound pulse [77]. The circulating microbubbles will re-establish flow through the imaging area and the signal recovery from the contrast agents are tracked using a recovering exponential model [77]. The time-constant associated with this recovering exponential is the “re-fill rate”, and correlates with the tissue perfusion rate. In the present paper, instead of using microbubble contrast destruction-reperfusion methods, we instead use tissue compression and monitor reperfusion of blood using photoacoustic imaging. Similar to the destruction-reperfusion approach, we fit the replenishing blood flow signal to a recovering exponential model to estimate the re-fill rate. It should be understood that the volume of tissue which is monitored, like the destruction-reperfusion technique, may not be well-defined. However, relative reperfusion maps are still possible and may provide valuable data which correlates with tissue perfusion.

Photoacoustic imaging is a preclinical technology that enables a label-free method of visualizing various chromophores in the body, which includes but not limited to, oxy- and deoxy-hemoglobin, amino acids and melanin. Being able to locate, image and differentiate oxy- and deoxy-hemoglobin allow the imaging technique to visualize vascular networks and quantify oxygen saturation within vessels [84, 85, 36]. Furthermore, Doppler shift can occur for acoustic signals generated by moving chromophores, which can be used to determine the rate of blood flow [38, 86, 40]. Ultrasound Doppler methods have likewise long-been used to estimate blood flow velocities in vessels. However, to date no label-free ultrasound or photoacoustic technique has demonstrated the ability to estimate tissue perfusion rates in bulk tissue volumes involving many sub-resolvable or undetectable vessels.

Our label-free method uses an ultrasound-photoacoustic (US-PA) dual imaging system to measure the perfusion rates in peripheral regions by pressing on the skin surface directly using the imaging transducer head. Due to the high resolution of PA imaging, we are able to detect net signals from tissue microvasculature, even if the vessel networks are not resolvable, allowing us to quantify changes in PA signals during compression and release. We fit the recovering mean photoacoustic signals to a first-order negative exponential model to create spatially-resolved images which quantify perfusion rates. Perfusion-rate differences are seen in various cold- and hot-water-bath exposure conditions.

## 5.2 Methods

### 5.2.1 Imaging System

Changes in capillary beds induced by compressions are imaged using the VEVO LAZR platform (Fujifilm, Visualsonics Inc.), a real-time US-PA dual imaging system. For this experiment, we used a LZ-550 transducer, which has a receive bandwidth of 32-55 MHz. Photoacoustic imaging is performed with 805 nm light delivered through a fiber bundle from the VEVO LAZR Optical Parametric Oscillator at the frame rate of 5 Hz. The laser power is 17 mJ/cm<sup>2</sup>, which is much lower than the ANSI safety limit of 32 mJ/cm<sup>2</sup> on the human skin and the frame rate is fast enough to detect PA signal changes during reperfusion as capillary refill time in a healthy finger is known to be slightly under 2 seconds. This wavelength is selected because it is an isosbestic point where the molar extinction coefficient of oxy- and deoxy-hemoglobin are the same. At isosbestic point, the absorption coefficient for oxy- and deoxy-hemoglobin is equal, allowing for unbiased signatures from blood vessels with variable blood oxygenation. As shown in figure 5.1 below, when a soft tissue layer is compressed, blood is excluded from the compression volume, reducing the PA signal in the compressed

---

area. The magnitude of loading rate is not measured nor it is constant. However, the load is measured by a force sensor (iLoad mini<sup>TM</sup>, LoadStar Inc.) in order to maintain a maximum compressive pressure of 50 kPa for full ejection. The transducer is fixed to a transducer holder mounted on a stage, as shown in figure 5.2b) for vertical compression. An example of sensing compression force synchronous with tracking the PA signal is shown in figure 5.2c). Once the transducer is placed on the hand, where the area (20 mm by 5 mm) is marked as shown in figure 5.2a), it will not change its location for the duration of the experiment. In addition, a custom-made standoff pad ( $\sim 5$  mm) cut from a large ultrasound gel pad (Aquaflex<sup>®</sup>, Parker Laboratories Inc.) is placed within the transducer head casing to allow uniform pressure distribution along the area of compression. Analogous to US perfusion imaging with contrast agents, the recovering PA signals after compression is released will be fit to a negative exponential model, allowing us to quantify the perfusion rates.

### 5.2.2 Human Subject Imaging Study

In order to assess the change in perfusion rate, cold- and hot water immersion tests are performed where the hand of a human subject is submerged in 4°C and 45°C water baths for various durations and the transducer head is used to directly compress on the hand in order to capture re-fill of blood vessels. The length of each compression-release (C-R) cycle is up to 10 seconds long with an interval between each cycle. The length of the interval time is set so that the durations of the C-R cycle and the interval time sum up to 30s. Up to 3 cycles are performed. Human subject experiments were conducted in accordance with ethical protocols approved by the University of Alberta Health Research Ethics Board (Pro00007759).

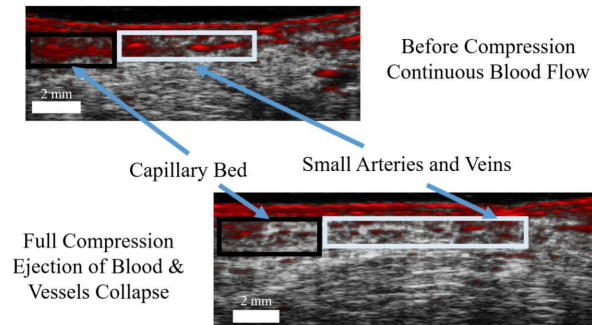


FIGURE 5.1: PA signals of the blood before and during full compression

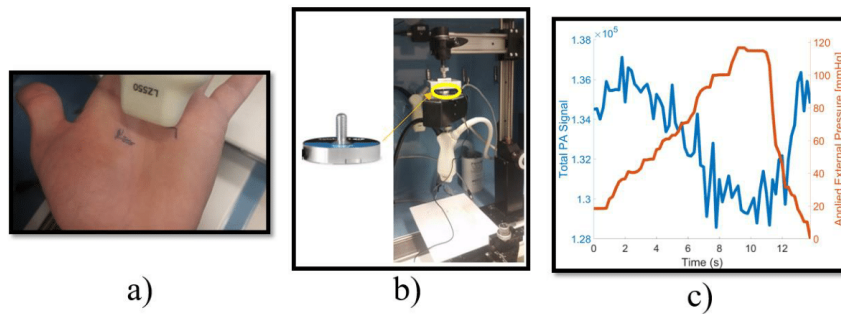


FIGURE 5.2: a) location of the transducer on the hand, b) the transducer fixed on the top along with the force sensor. The transducer and the force sensor are restricted to a vertical movement and c) an example of PA signal tracking synchronized with pressure sensor reading

### 5.2.3 Analysis Method

To demonstrate differences in re-fill rates of tissues subjected to temperature variations, we imaged a human palm in water immersion baths with different exposure times and temperatures as noted above. Perfusion-rate images were formed using the ultrasound and photoacoustic imaging data using the fitting methods described above.

As shown in figure 5.3a), on an initial image, a region of interest (ROI), marked by a yellow line, is chosen to define the boundary where the perfusion re-fill rate estimation will be performed. Within the chosen ROI boundary, a smaller ROI, which is denoted as a "sliding window", shown as a green rectangle in the same figure, is defined. Mean PA signals inside the sliding window at each frame will be directly tracked. Note that the region of tissue associated with a sliding window may change in effective area as the tissue is compressed. We ideally want this sliding window to sample the same tissue volume during each stage of compression. Otherwise, vessels may move in or out of the window during compression, creating unwanted variation in the mean photoacoustic signal. For this reason, we use ultrasound data to track tissue motion to adaptively change the sliding window size to ensure that the same volume of tissue is being measured at each stage of compression.

For this reason, we first separate each image into its respective US and PA components and use ultrasound data to track tissue motion to adaptively change the sliding window size to ensure that the same volume of tissue is being measured at each stage of compression, as shown in figure 5.3b). Using a robust US strain estimation algorithm AM2D by Rivaz et al. [87], the RF signal of the B-scan at specific frame and the frame immediately after the chosen frame are processed to estimate both the axial and lateral displacement of the tissue, creating an ultrasound deformation map. The map is applied on the sliding window to create warping.

After PA tracking in a sliding window, started in a specific location is completed, the tracking analysis repeats from the first frame with the sliding window starting from a new location bounded by ROI, denoted by a blue arrow in figure 5.3a). Also, AM2D only needs to run once as deformations are estimated on the entire image area. This process is repeated until the starting location of the sliding window covers the main ROI, the yellow boundary.

During the tracking using MATLAB, large vessels greater than  $\sim 500 \mu\text{m}$  (as measured with a 40 dB threshold) were detected and excluded from further PA analysis. This is to prevent flow rates from large vessels skewing the tissue perfusion rates as large vessels have much faster flow rate than arterioles and capillaries and they may be less effected by external temperature changes, which hinder accurate analysis of the perfusion rates of smaller vessel networks.

To estimate the perfusion rates, a negative exponential equation, shown in equation 5.1, is used to model the PA signal recovery after the tissue is released from external loading:

$$S = A(1 - e^{-t\rho}) + S_{min}, \quad (5.1)$$

where  $S$  is the current PA signal strength,  $A$  is the PA signal difference between the steady state and the maximum-applied-compression,  $S_{min}$  is the minimum PA signal, which occurs at the maximum compression, and  $\rho$  represents the re-fill rate. The beginning of the release of compression is determined by the ultrasound strain map image sequence <sup>1</sup>.

### 5.3 Results

To demonstrate differences in reperfusion rates of tissues subjected to temperature variations, we imaged a human palm in water immersion baths with

<sup>1</sup>The video can be found on the SPIE publications website once it is published

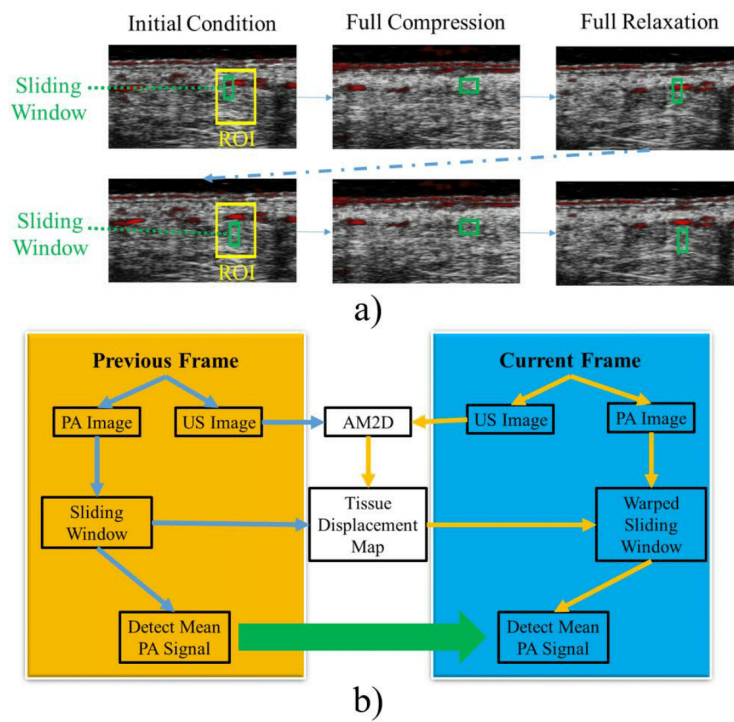


FIGURE 5.3: Schematic of reperfusion rate analysis: a) placement of the ROI and sliding window in the initial frame and the warping of the sliding window that correlates to the tissue movement. b) Overview of how PA signals are measured and tracked over multiple frames.

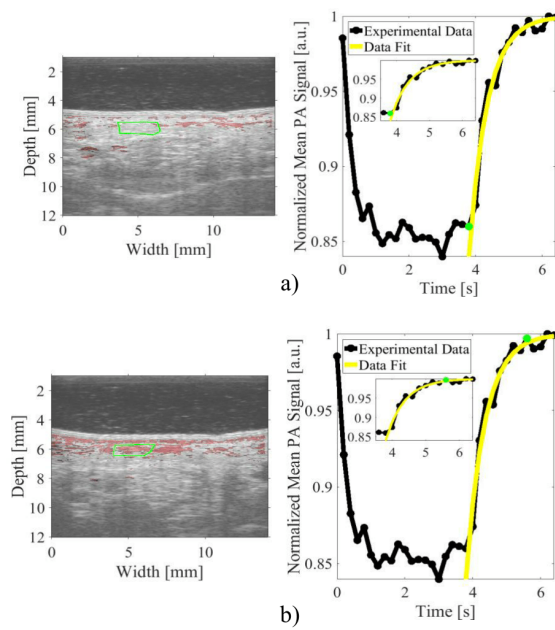


FIGURE 5.4: The Transformation of a Sliding Window a) During Slight Relaxation and b) Full Relaxation Using Displacement Estimated by AM2D. The small plots within the large plots are magnified version of the large plot.

different exposure times and temperatures as noted above. Perfusion-rate images were formed using the ultrasound and photoacoustic imaging data using the fitting methods described above.

The distribution of perfusion rates within the main ROI when the hand is submerged in the cold and hot water baths are shown in figures 5.5. Clear differences in the perfusion-rates are seen between differing temperature exposure conditions as visualized by the red-to-blue colormaps with red and blue colors representing fast and slow re-fill rates respectively. Here the size of the main ROI is 6.21 mm wide by 3.25 mm deep, and images in figure 5.5 had a sliding window size of 4.24 mm by 0.78 mm to detect changes in PA signal. To explore how window sizes affect perfusion-rate estimates as larger window for averaging tends to reduce effect of noise, additional window size of 2.83 mm by 0.78 mm 1.41 mm by 0.78 mm, and 0.78 mm by 1.95 mm respectively, are used and compared in Fig. 5.6. For 30s, 60s and 90s that the hand was submerged in the 4°C water bath, the mean re-fill rate constant range from 0.28s<sup>-1</sup> to 0.38s<sup>-1</sup>, 0.29s<sup>-1</sup> to 0.34s<sup>-1</sup> and 0.14s<sup>-1</sup> to 0.22s<sup>-1</sup> respectively. In contrast, when the hand is submerged in a 45°C water bath for 0s 30s and 60s, the mean re-fill rate constant range from 0.53s<sup>-1</sup> to 0.56s<sup>-1</sup>, 0.84s<sup>-1</sup> to 1.16s<sup>-1</sup> and 1.15s<sup>-1</sup> to 1.59s<sup>-1</sup> respectively, depending on window sizes. The mean re-fill rates are listed in table 1. The exposure time shown in figure 5.6, denotes the start time for each C-R cycle. The standard deviation of the perfusion rates vary with window size and is smallest when the sliding window is 1.41 mm by 0.78 mm.

## 5.4 Discussion

We have demonstrated a new method to image the perfusion rates in superficial tissues using a non-invasive, label-free, US-PA imaging system. Statistically-significant differences using paired t-tests were observable ( $p < 0.05$ ) in mean

Window Size Depth x Length (mm X mm)	Water Temp	Mean Refill Rate ( $s^{-1}$ )					
		4°C			45°C		
	Submersion Time	30s	60s	90s	0s	30s	60s
4.24 x 0.78		0.31	0.37	0.14	0.59	1.18	1.56
2.83 x 0.78		0.34	0.33	0.18	0.57	0.97	1.26
1.41 x 0.78		0.32	0.29	0.19	0.55	0.91	1.2
0.78 x 1.95		0.5	0.31	0.22	0.56	0.87	1.27

TABLE 5.1: The estimated mean re-fill rates. The submersion time is the duration the hand was submerged in a water bath before the start of the compression

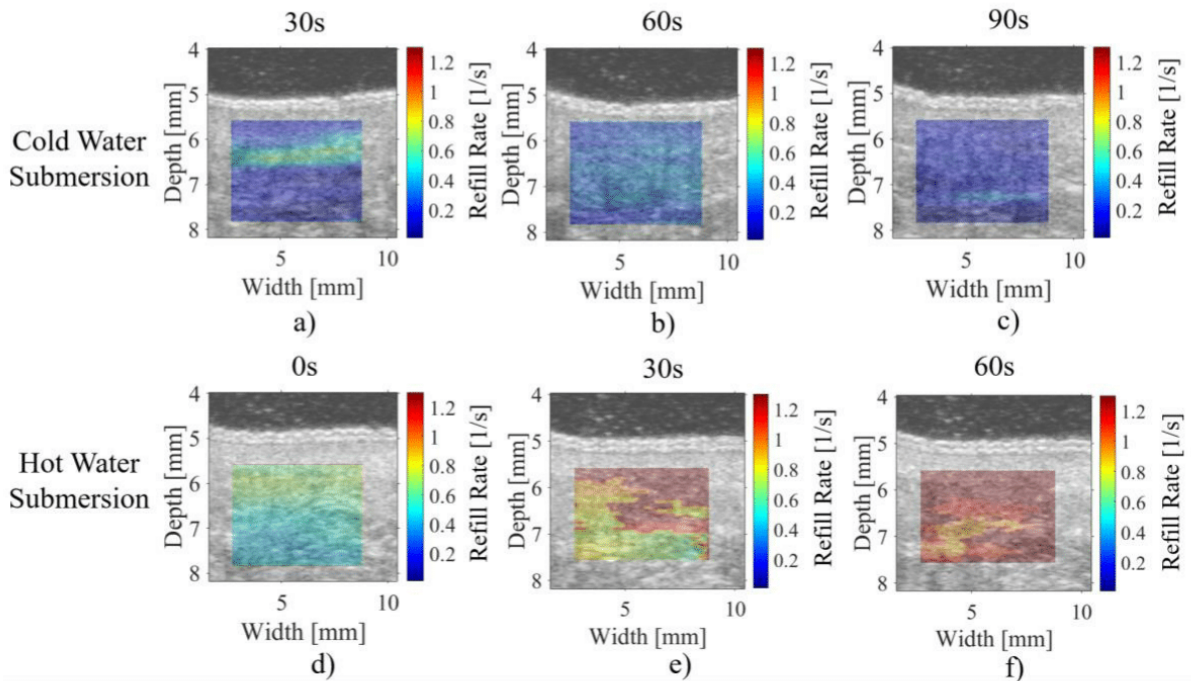


FIGURE 5.5: The re-fill rate distribution of the left hand of a human subject in the a)-c) 4°C water bath for 30s, 60s and 90s respectively and d)-f) 45°C water bath for 0s, 30s and 60s respectively. Times shown above each image denote the exposure time at the start of each C-R cycle. The size of sliding window is 4.24 mm wide and 0.78 mm long

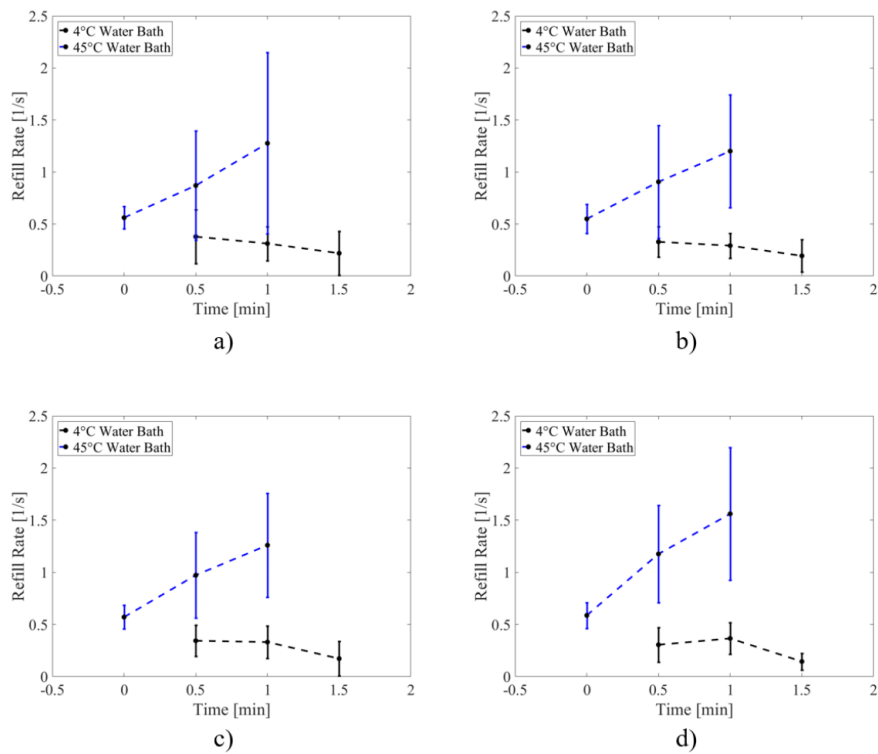


FIGURE 5.6: The average perfusion rates with different sliding window sizes as a function of exposure time in the hot- and cold water baths. Sub-figures are for the following initial sliding window sizes. a) 4.24 mm by 0.78 mm b) 2.83 mm by 0.78 mm, c) 1.41 mm by 0.78 mm and d) 0.83 mm by 1.95 mm

perfusion-rates in multiple cold and hot temperature-exposure conditions. In addition, the distribution of perfusion rates in superficial tissue up to several mm depth can be estimated. Lower-frequency probes and higher-power light delivery could enable depths of multiple cm in future work.

The ultrasound-photoacoustic system is capable of additional imaging modes such as color Doppler and Power Doppler. In principle Power Doppler could potentially be used to estimate the changes in flow associated with re-fill after release of compression. However, when tissue is compressed or released, the flow signal from vessels are overwhelmed with the Doppler signal from tissue motion. This takes several seconds to recover, which is too long considering that the capillary refill occurs within a couple of seconds.

The variance of the perfusion-rate estimates increases with increasing body temperature. This may be due to the fact that fewer data points exist on the recovering exponential fit when the reperfusion rate is high. Errors in displacement estimation impact how a given region of tissue deforms and thus impacts the associated window deformation for analysis. Future work should investigate the impact of errors in this changing window size. Using an imaging system with higher frame rate will improve the temporal resolution of the perfusion rates and will permit faster compression-release cycles. Future work should investigate optimal sliding window sizes, optimize for large-vessel rejection, and push limits of depth and frame-rate. Furthermore, more careful analysis from larger sets of data should be performed. Reperfusion rate measurements using ultrasound perfusion phantoms and *in vivo* studies involving multiple human subjects must be performed, which may improve data sensitivity and yield more accurate results.

Perfusion-rate estimation method used in this paper deals with photoacoustic signal that are detectable but are spatially unresolvable. The large standard deviation may be due to the low SNR of unresolvable signals. In addition, the

hand was not restrained during the measurement and the human subject had to intentionally focus on keeping the hand still. For future works, a laser system with higher power delivery and higher frequency transducer will allow improved SNR for small vessels, allowing more accurate analysis of perfusion-rate estimation.

As tissue is compressed, both acoustic and optical properties of tissues may be impacted [88]. Applied pressure may also exclude blood, lowering the net absorption, while effective distance to vessels will decrease. Thus compression may alter effective fluence at vessel locations. Currently, the present analysis ignores such effects but future work should aim to better incorporate these effects for more quantitative perfusion-rate estimation.

The negative exponential model for calculating the perfusion rate,  $\rho$  is analogous to the wash-in rate (WIR) of contrast agents used in various contrast-enhanced perfusion imaging techniques. Future work could compare our label-free compression-reperfusion method with contrast-based perfusion imaging techniques. However, it is anticipated that quantitative perfusion rates from our approach may not necessarily match reperfusion rates from contrast-based approaches. For example, the WIR of destruction-reperfusion contrast ultrasound may depend on the thickness of the elevational beam waist, among other considerations. The WIR of our compression-reperfusion PA imaging will largely depend on the size of the compression area and internal pressures may be depth dependent. Future work should investigate these issues and correlate our label-free approach with contrast-enhanced methods.

Label-free perfusion imaging could have a significant role in assessing tissue health in a number of diseases, including diabetes, cancer and etc [81, 68, 82]. Dynamic Contrast-Enhanced MRI has show significant potential for discriminating malignant from healthy tissues in a range of cancers including breast cancer and prostate cancer. However, it's expense and the necessity of contrast

injections preclude it from widespread screening applications. Our approach is not only label-free but potentially high-throughput and relatively low-cost. Future work should investigate deeper tissues and various cancers and disease models.

Viscoelasticity of the soft tissue may introduce tissue relaxation that can re-open vessels during the compression phase. However, the impact of these effects should be minimal as compression and relaxation are performed on timescales faster than tissue viscoelastic relaxation rates, typically several seconds [89, 90, 91]. Future work should investigate the impact of tissue viscoelastic properties on perfusion-rate estimation and account for heterogeneity in tissue mechanical properties.

## 5.5 Additional Discussion

The experiment assumed that the photoacoustic signal recovery is linearly related to the amount of blood re-flowing through small vessels. However, the actual relation between the two quantities are unknown. Therefore, further studies must be done to understand how blood flow in vessels of various sizes are related to the received photoacoustic signal. Then the relationship will be used to further correct the estimation of reperfusion rate.

## 5.6 Conclusions

We have demonstrated a new label-free imaging method for mapping perfusion-rates of tissues using compression-release photoacoustic and ultrasound micro-imaging. Given its real-time and label-free nature, the approach could have significant value in clinical settings where high throughput screening is desirable.

## **Disclosures**

The authors have no relevant financial interests in this article and no potential conflicts of interest to disclose. R. Zemp is Chief Scientific Officer and Co-Founder of illumiSonics Inc., which, however, did not support this work.

## **Acknowledgments**

We gratefully acknowledge funding from NSERC (355544-2008, 375340-2009, STPGP 396444), Terry- Fox Foundation and the Canadian Cancer Society (TFF 019237, TFF 019240, CCS 2011-700718), Alberta Innovates Health Solutions AIHS CRIO Team Award 201201154, the Alberta Cancer Research Institute (ACB 23728), the Canada Foundation for Innovation, Leaders Opportunity Fund (18472), Alberta Advanced Education and Technology, Small Equipment Grants Program (URSI09007SEG), and Alberta Ingenuity / Alberta Innovates scholarships for graduate and undergraduate students.



## Chapter 6

# Estimation of Vessel Internal Pressures with Tissue Deformation

### 6.1 Introduction

Being able to quantify blood pressure in vessels is of critical importance as blood, which is necessary for the exchange of oxygen, nutrients and waste materials between tissue cells and blood, requires pressure gradients to flow throughout the body. In clinics, sphygmomanometry is used as a first step to determine any systemic arterial pressure abnormality in the limbs. It is simple and inexpensive to use. However, it can only measure the pressure of the brachial artery or of the artery in the ankle. Sphygmomanometry does not have the ability to monitor blood pressure continuously as the measurement is performed by occluding vessels and the method may over- or under-estimate the pressure depending on the size of the pressure cuff. Other than sphygmomanometry, there is another method to measure blood pressure, which requires cannulation. It works by injection of cannulae needles or catheters intravenously to access other vessels or heart chambers, and it is often used in the intensive care unit for continuous real-time monitoring of arterial blood pressure. But, due to its invasive nature, the technique may cause infection and bleeding. Currently, there is no clinical method that can measure blood pressure in smaller vessels.

In previous chapters, *in vivo* pressure-area data were fitted against Shapiro's exponential model in order to estimate the internal blood pressure of the vessel. This model equation is a phenomenological model that has been proposed to fit data sets obtained from *in vitro* experiments and the extent of its applicability is unknown. It assumed a thin wall approximation so its validity *in vivo* is

uncertain. In addition to this model, two additional models are proposed which potentially relax the thin-wall constraint. To test the validity of these models, we construct 3D finite element models (FEM) of a thick-walled tube and a human arm using the commercial finite element simulation software ABAQUS. We fit proposed models to the FEM data to investigate the applicability of using the models for internal pressure and tissue mechanical parameter estimation.

## 6.2 Finite Element Model Description

We use finite element modeling to computationally simulate two scenarios: one is a thick-walled tube and the other one is a human arm with a single, low-blood-pressure vessel and a bone located in the center. We also modeled a thin-wall model, which agreed with the Shapiro model, however, this will not be discussed here for brevity. With each model there are two methods of loading: the first method is applying uniform pressure on the boundary, mimicking the application of a pressure cuff and the second method is to model a top-loading case, which is to model experiments in previous chapters that had an ultrasound transducer pressing down on the skin surface directly. Hence, there are four different Finite Element computational model scenarios in total. In addition, different vessel sizes and different tissue mechanical properties were considered.

While a simulation model for a thick-walled tube can be easily set up, modeling a human arm accurately is extremely difficult due to its mechanical heterogeneity and complex geometries. Some simplifications are made to achieve a balance between accuracy and computational cost, which are discussed below. Furthermore, veins are modeled as a wall-less vessel. It is assumed to be wall-less because of the lack of smooth muscle, which makes the vessel integrity weaker and its mechanical property more comparable to the surrounding soft tissue. In addition, the vessel walls of veins are thinner than that of the artery and are considered to be negligible compared to the overall dimension of the entire arm [92].

When setting up the FEM simulations, symmetrical characteristics may be exploited to further increase computational speed. For the thick-wall and the human arm models, symmetry allows the FEM to be simplified by 1/8 and 1/4 of the original size, respectively. However, preliminary results have shown that

some of the symmetries in the original configurations are lost in the deformed configurations. Only the out-of-page (z-axis) symmetry, explained in figure 6.1, was retained. Hence, the models used in the simulations are partially simplified according to the retained symmetry.

### 6.2.1 Geometry

The FEM simulations are modifications from the setup by Lan et al. Figure 6.1 shows a cross-section of two FE models used in this experiment with labeled dimensions. For both models, the size of the outer radius is fixed at 52 mm and the radius of the vessel is fixed at 0.1 mm, 0.5 mm or 2 mm. The distance between each node is set to be a quarter of the radius. The total length of the arm is set to be 24 cm, meaning only half, 12 cm, of it is used for the simulation. For simplification, the soft tissue in the arm is considered to be homogeneous. For a thick-wall tube model, veins are assumed to be embedded in the center of the arm. But for the human arm model, the center of the vein is located 7 mm from the outer surface in order to mimic compression of small vessels located in superficial tissue regions. For the case of uniform compression, radial load is applied on the middle half of the outer surface (12cm) in the original, unreduced model. Similarly, the length and the width of the compression area in the case of top loading are 19.05 mm and 5 mm, respectively. The areas of compressions are shown in figure 6.2, denoted by pink arrows.

The main constituents of the human arm are skin, fat, muscle, bone and vessels. However, even in the case of material heterogeneity, muscle tissues are known to behave as a linearly isotropic elastic material that have similar quality to fat and skin when the strain is under 10% [93]. Therefore we have used the Young's modulus of 47.5 kPa for the simulations. However, because Young's modulus of the human arm is known to change depending on the applied strain, models with two other Young's moduli, 40 kPa and 55 kPa, are tested. Bone, in comparison to other tissues, have much higher Young's modulus (10 MPa). Therefore, it can be assumed rigid. The venous walls are divided into three layers, that are known as intima, media and adventitia. Each layer is made of different proportions of collagen and elastin. While vessels walls are anisotropic due to their composition, there is not sufficient information in order to be used for the simulation. Therefore, it is assumed to be isotropic, which is still known

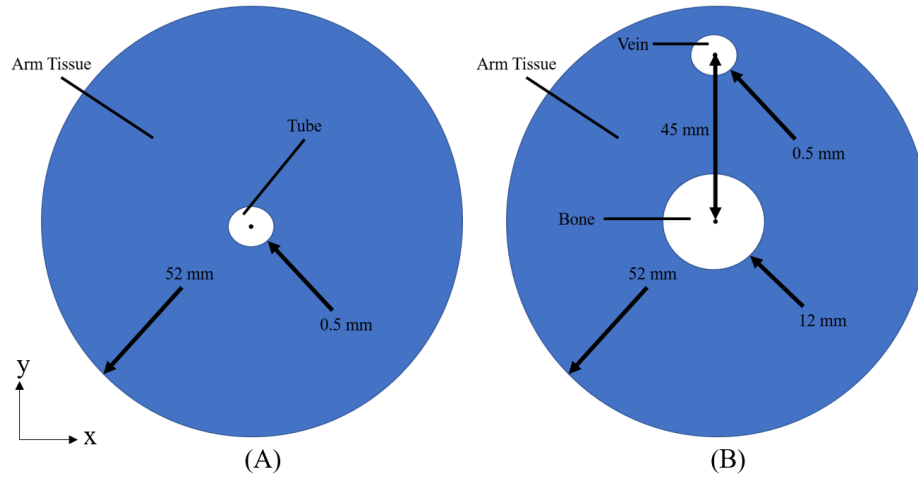


FIGURE 6.1: The dimensions of the cross-sections of (A) tube wall model and (B) human arm model, z-axis is directed out-of-page

to give satisfactory results [93]. The soft tissue in the human body is considered to be nearly incompressible so the Poisson's ratio is set at 0.45 [93].

For the thick-walled tube model, the two ends are fixed to prevent them from displacing. In addition, the bottom of the cylinder is fixed when the loading is applied from the top. For the arm model, we assume it stays rested and is still during the measurement and for the purpose of improving computation, the bone is not modeled but only its boundary defined and fixed. The ends of the arm model are not fixed for more realistic modeling. Also, the bottom is not fixed when loaded from the top as the rigid bone restricts any downward movement. The various boundary conditions and the loading areas are shown in figure 6.2. Note the boundary conditions are denoted by orange and blue marks that represents zero displacement and rotation conditions, respectively.

When loading is applied, it is applied as a ramp and dynamic simulations, a type of simulation dependent on time varying behavior of the material, are performed until a vessel first collapses. Here tissue viscoelasticity and anisotropy are ignored for simplicity but should be accounted for in future work. Large displacement simulations were performed. The ramping rate was set so that all vessels collapse within 0.8s. Internal pressures were applied on the vessel walls, and they were kept constant through the simulations. Pressures, both internal

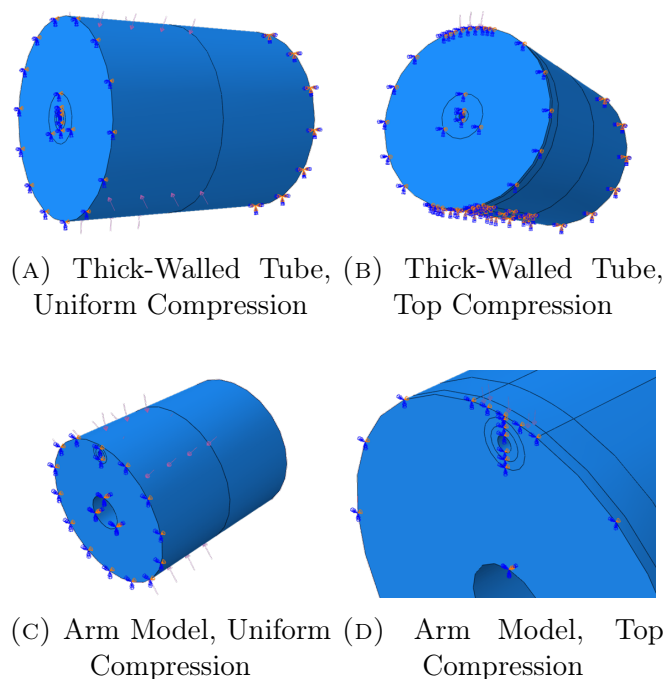


FIGURE 6.2: Various views of the Four Simulation Models

and external, are given as forces per unit area.

### 6.3 Fitting Models

The exponential model first provided by Shapiro as given in Eq. 2.1 can only be applied within the "similarity range". This range is defined where the normalized cross-sectional area is smaller than when the vessel cross-section makes a line contact as shown in Fig. 2.2. This is also applicable for a thin-walled model in *ex vivo* vessel experiments. As the normalized cross-sectional area increases, the fitting starts to diverge due to the asymptotic behavior of the exponential model, which incorrectly predicts that the normalized cross-sectional area extends to infinity as the transmural pressure approaches zero. However, Shapiro also proposed a modified exponential model, which provides a better fit over a larger range, where the normalized area,  $\alpha = A/A_0$ , is less than 1. The modified model is

$$-\frac{p_i - p_e}{\kappa_p} = \alpha^{-n} - 1 = \left(\frac{A}{A_0}\right)^{-n} - 1 \quad (6.1)$$

Here  $p_e$  is the external loading pressure,  $p_i$  is the internal pressure within the vessel,  $n$  is an exponential factor to be fit, and  $\kappa_p$  is the parameter proportional to the bending stiffness of the tube wall also known to be the critical pressure of vessel collapse. The only modification is the addition of the -1 term on the right hand side of the equation. This shifts the location of the asymptote so it occurs when external pressure is equal to  $\kappa_p$ .

One additional model, termed the 'quadratic model' is derived from constitutive equations for an axially symmetric linearly elastic circular cylinder and used for fitting. Derivation of the model, which is included in the appendix, shows the normalized area  $\alpha$  is related to the external pressure by the following equation:

$$\alpha = \left[1 - \frac{2(1 - \nu^2)p_e}{E + (1 + \nu)p_i}\right]^2 \quad (6.2)$$

where  $p_e$  and  $p_i$  are external and internal pressures, respectively,  $\nu$  is the Poisson's ratio and  $E$  is the Young's modulus. This model assumes that both induced strain and displacements are small and that the vessel retains its circular shape while it is being loaded.

## 6.4 Fitting Methods

Overall, the change in normalized cross-sectional lumen area due to increasing external pressure can be divided into 2 regions, pre-buckling and post-buckling regions. However, for the quadratic model, the pre-buckling region can be further divided into small- and large-strain regions. Here we define small strain as less than 5%. After each simulation, the data was exported and the cross-sectional area was calculated using MATLAB and plotted against the applied pressure for the uniform loading case. For the top loading case, the simulation outputs pressures at each node point on the boundary of the vessel and these values are averaged then used in the place of the applied pressure for plotting. This is because the pressure applied at each node on the vessel wall has non-negligible differences in this situation.

## 6.5 Results

When comparing the data from FEM simulations for different-sized vessels, the normalized area versus loading curves showed negligible differences in the goodness of the fit and in the estimation of parameters. In light of such outcome, the stated results for each type of simulation, stated below, holds true to all three vessel sizes. For consistency, reported figures and data are samples of FEM simulations for the vessel size of 0.5 mm.

### 6.5.1 Thick-walled Tube with Uniform Loading

As pressure is increased, the shape of the tube appears to be maintained until the inner cylinder buckles. Unlike the prediction in the buckling of thin-walled tubes by Shapiro, the tube does not make a point contact after buckling. Instead, post-buckling is characterized by contact first occurring at two ends of the vessel cross section, rather than the center. The inward pinching then continues until it creates a line contact as shown in figure 6.3. This could be an artifact of discretization, however, when increasing the node density, a similar behavior occurred.

When fitting the data from the case of a centered vessel with uniform loading, the quality of the fitting exponential model in the pre-buckling region is good as shown in figure 6.4. By buckling, we mean that the vessel cross-sectional shape first loses stability in at least one location. Despite the good fit, the estimated parameters are complex-valued and inaccurate. For uniform pressure applied in the thick-walled tube, buckling occurs when  $\alpha$  is around  $0.15 \sim 0.2$ . While the quality of the fitting seems to be less accurate in the post-buckling region than the pre-buckling region, the estimated parameters are real-valued albeit much higher than values used in the simulations as comparisons are shown in table 5.1.

The modified exponential model fit to the data in the pre-buckling region has similar quality as the model fit shown above using the exponential model. However, the estimated parameters are all real-valued. A sample of estimated values shown in table 6.2 reveal that estimated internal pressures are mostly under-estimated in comparison to the pressures used in the simulation. One

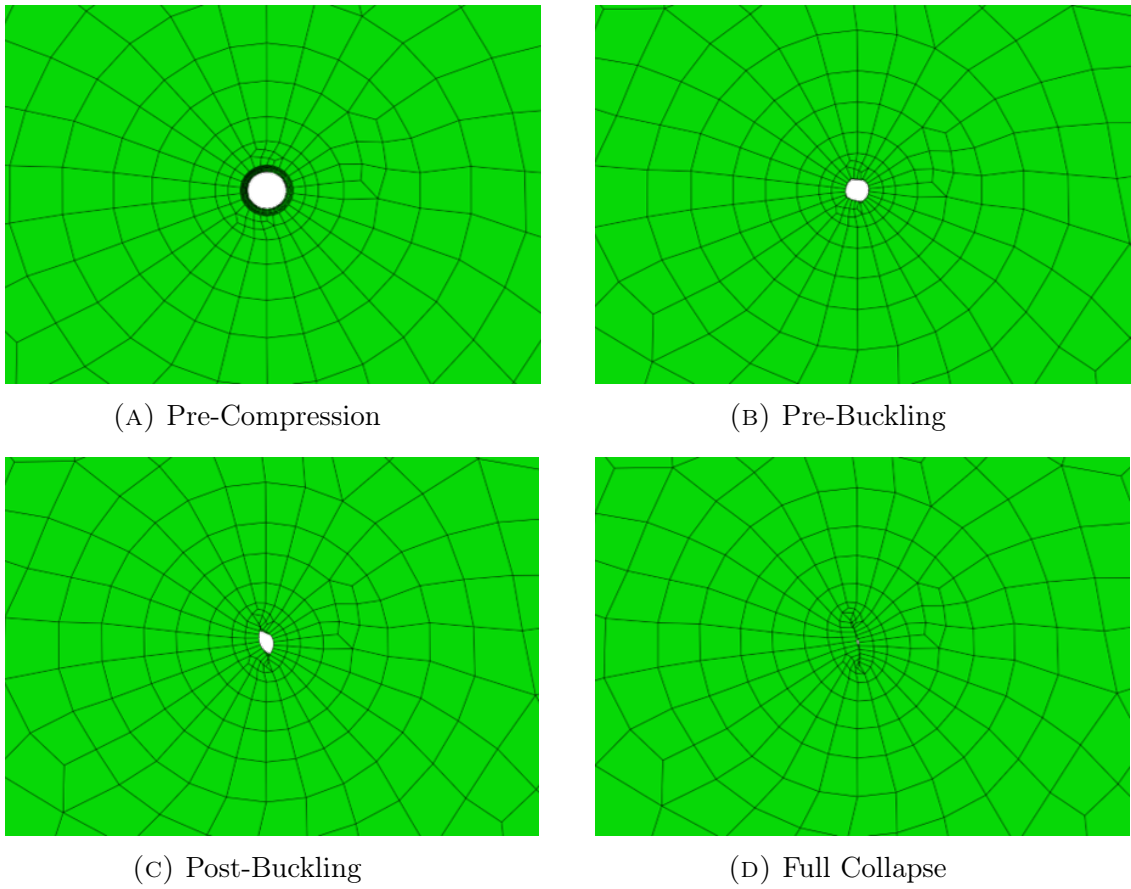


FIGURE 6.3: A sample of fitting on results from FEM simulation of a thick-walled tube.

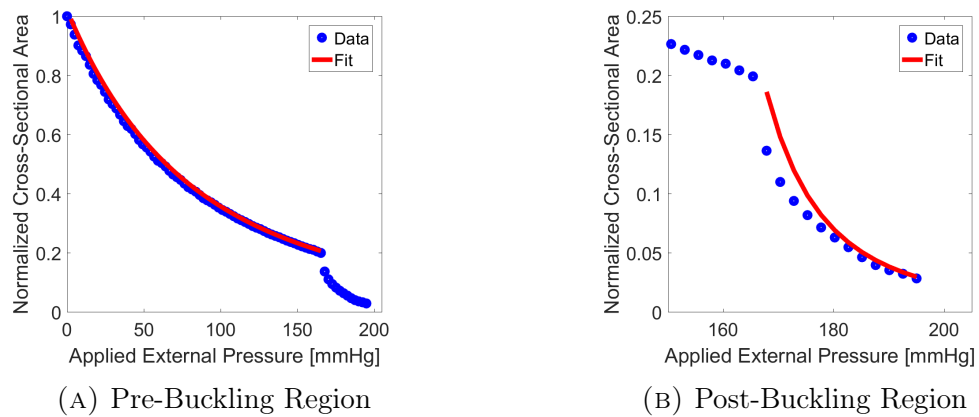


FIGURE 6.4: A sample of fitting on results from FEM simulation of a thick-walled tube.

notable behavior is that the increase in internal pressure set during the simulations translates to increase in pressure estimates and therefore, the exponential model is able to estimate relative pressures qualitatively but not quantitatively. The quality of the fitting on a post-buckling region is poor and the estimation completely inaccurate.

The quadratic model shows an extremely good fit and produces accurate estimation of parameters in the small-strain region as shown in figure 6.5. In addition, table 6.3 shows the detected internal pressure, Young's modulus and Poisson's ratio are all within 15% relative error. The estimation seems to deviate with large internal pressures in which case all three parameters are underestimated. In contrast, the quadratic model shows a poor fit in the large-strain region and it is worse in the post-buckling region as shown in 6.6. The simulated strain at maximum compression is high as well, reaching close to 60%.

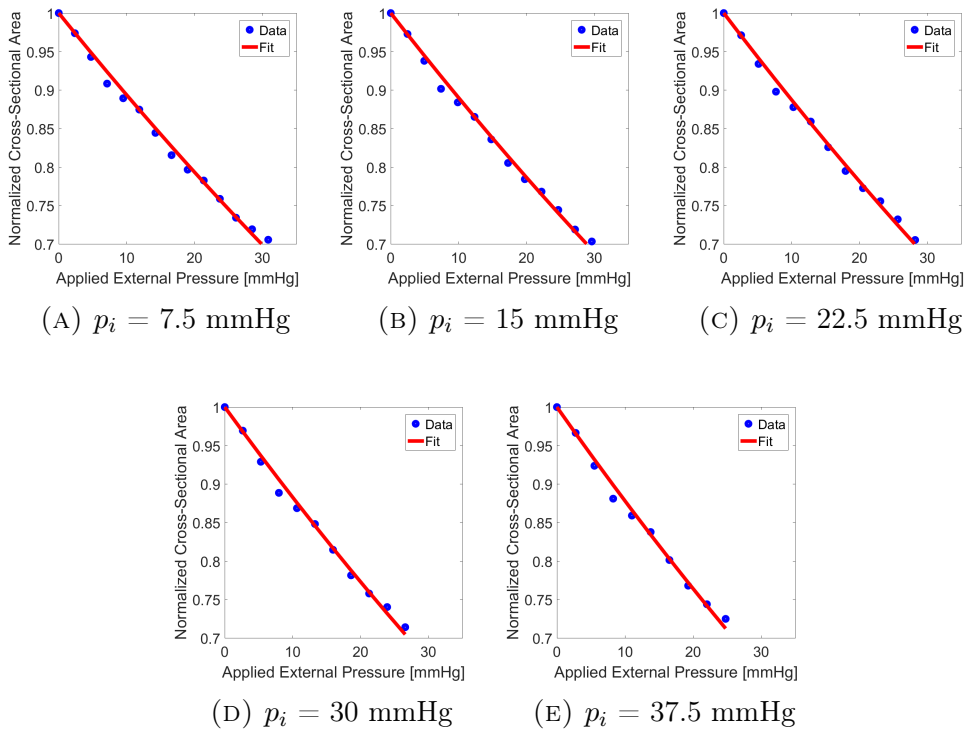


FIGURE 6.5: Data Fitting using Quadratic Model on a Small Strain Region with Young's modulus of 40 kPa

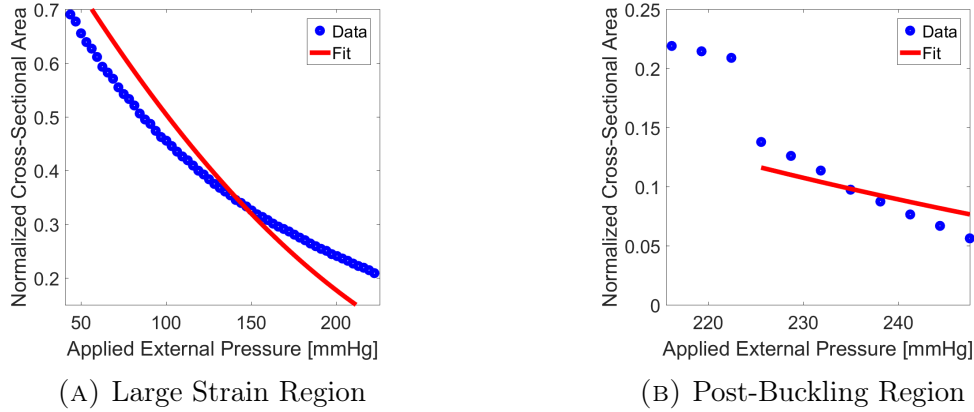


FIGURE 6.6: A sample of fitting on results from FEM simulation of a thick-walled tube using a quadratic model.

### 6.5.2 Centered Vessel With Top Loading

Unlike the uniform loading case, the pressure-data relationship cannot easily be divided into pre-buckling/post-buckling (or small/large strain) regions as the top surface of the FEM deforms too much before vessels approaches the point of buckling. The FEM software aborts most likely due to the coarse mesh on the outer boundary compared to the finer mesh on the vessel. However, the applied external pressure is already much greater than the internal pressures before the simulation aborts and making the mesh finer on the outer boundary would cause the simulation time to be exponentially longer, which is not recommended. The induced strain at the vessel boundary at the maximum deformation at the top surface is around 5%, which is considered small. The quality of the normalized area versus loading plots, in comparison to the case for uniform loading, are more noisy. Furthermore, the applied local pressure, calculated by averaging the pressure on the vessel boundary, is extremely low,  $<3$  mmHg due to the top and bottom of the vessel exerting compressive force while both sides are exerting tensile force (not shown).

The exponential model, similar to the uniform loading case, estimates complex-valued parameters but with poor fitting quality. Also, the modified exponential model provides a similar fit. However, setting higher internal pressures in the simulations does not result in an increase in estimated internal pressures. Furthermore, other parameters do not seem to reveal any correlations as well.

The quality of the fit using the quadratic model is shown in figure 6.8. Other than the fitting on fig.6.8(D), which shows the curve that is located slightly below the data points, other plots seems to suggest good fits. The deviation in estimation seems to increase from 1.74 mmHg to 16.10 mmHg as the internal pressure set in FEM is increased from 7.5 mmHg to 37.5 mmHg for successive simulations. While the estimated Poisson's ratios are, although under-estimated, close to the value used to set up the FEM, the estimated Young's moduli are slightly greater than half of the values used in FEM.

### 6.5.3 Arm Model with Uniform Loading

Unlike the trend shown in the case of centered vessels with uniform loading, the trend in the reduction of normalized area for the modeled human arm is characterized by a gradual decline without an obvious change in the curve associated with buckling. Also, the increase in external pressure leads to buckling when the vessel is close to having a zero normalized area, which, when added with the characteristic of gradual decline, results in buckling becoming undetectable. A vessel in the arm model is able to retain its shape and becomes more elliptical with increasing load instead of having it buckling. Because of the aforementioned facts, the fitting was performed using small- and large-strain regions and the entire data. The normalized area,  $\alpha$ , is 0.6 when the strain is  $\sim 5\%$ .

Using the exponential model, fittings in both small- and large-strain regions separately show poor fits, which makes the estimated values to be unreliable and of no significance. When the same model was used to fit the entire data, the fitting seems to be better but the estimated parameters are still complex-valued. Therefore, the exponential model cannot be used as an estimation technique for this geometry.

As shown in figure 6.9, data fitting using modified exponential model shows the best fit before induced strain exceeds 5%. However, the estimated internal pressures are between 0 mmHg and 21.2 mmHg and they do not show any correlations to the internal pressures set in simulation models.

The quadratic model, in comparison to the other two models, shows good fits over the entire range of applied compression as a sample plot is shown in figure 6.10. In addition, the estimated parameters are very close to the parameters used in FEM as shown in table 6.6. The minimum and the maximum relative

errors for internal pressure, Young's modulus and Poisson's ratio are 2.1%, 18.5%, 2.5%, 24%, 0.17% and 2.42% respectively.

#### 6.5.4 Arm Model with Top Loading

In the arm model where the the load is applied on top, the buckling of the vessel can be seen as the load is increased. Unlike the top loading in the thick-wall tube, the vessel is located closer to the outer boundary and the full deformation can be seen before the loaded surface deforms too much. A maximum of 370 mmHg of pressure can be loaded on the top surface before the simulation cannot continue. In the current case, the vessel becomes elliptical and then starts collapsing from the side, similar to the uniform loading on a thick-walled tube. At the maximum compression, the strain is calculated to be between 15% ~ 30% around the inner radius.

The fitting using the exponential model again shows that it is unsuitable for the estimation internal pressure and other mechanical properties. In contrast, the modified exponential model seems to provide a slightly better fit only when it is fitted in the small-strain region. But the estimated values for internal pressures are between 1.65 mmHg and 1.73 mmHg,  $\kappa_p$  between  $2.5 \times 10^5$  kPa and  $7 \times 10^5$  kPa and  $n$  between 0.06 to 0.1. Thus, there is no correlation with the pressures set in FEM and the estimated values.

The quality of fitting using the quadratic model is good in the small-strain region as shown in figure 6.11. Both the estimated internal pressures and Young's Moduli are under-estimated with relative errors between 45% to 60%. The estimated Poisson's ratios, however, are closer to the values set in FEM with relative errors around 6%. The comparison of results are shown in figure 6.7. For the top-loading case, while quantitative internal pressure estimation was not achieved, relative pressure estimation could be possible due to the monotonically increasing trend.

## 6.6 Discussion

The parameters estimated using the quadratic model seems to have yielded the closest results from all four FEM simulations. The results seemed to be

even better in the arm model than in the tube model. This may be due to the lower induced strain, which fits better to the small-displacement model assumption. While the predictions of internal pressure and Poisson's ratio are very close ( $<8\%$ ), the Young's modulus seems to be over-estimated in general and the estimation becomes worse with higher internal pressure. However, the Young's modulus cannot be compared directly as the simulations are setup in three dimensions while the estimation of Young's modulus is based on the cross-section of the 3D model. The fitting also seems to work over a larger region of data. For the thick-walled tube model, the fitting seems to be valid over a small region, where the strain is considered small. The fitting seems to deviate as the strain becomes larger, which is to be expected due to how the model was derived. However, that is not the case for the arm model as although the buckling of vessels in the arm model seem more gradual than the one in the tube model, the vessel do not retain its original circular shape as the load is increased. Even the induced strain is not so low ( $\sim 20\%$ ) before the vessel collapses and its wall starts pinching.

The exponential model did not work in most cases due to its characteristics. It is defined so that it has both vertical and horizontal asymptotes. The main issue lies in the fact that it assumes an infinite area when transmural pressure is equal to zero, or internal pressure is equal to external pressure. Since all of the data starts at the area of 1 with the external pressure of zero, which is equivalent to the negative transmural pressure, the model cannot match the data using real-valued parameters. The modified exponential model also has both vertical and horizontal asymptotes. However, the model predicts an infinite area when transmural pressure is equal to  $\kappa_p$ . Overall, data fittings have shown that the fits are good only when the estimated parameters are complex-valued, which only signifies the shortcoming of this Shapiro exponential model. Additionally, the exponential models do not work because they are based on the phenomenon of a thin-wall buckling. As the thin wall becomes elliptical, the dimension of the major axis is much greater than that of the minor axis, which would allow the middle of the ellipse to pinch. However, simulation models have thick walls, which means that the dimensions between the major axis and the minor axis are similar, resulting in a different behavior shown in figure 6.3.

Outside of fitting results, simulations have shown that vessels, whether centered or not, do not collapse when the internal pressure is equal to the external pressure. This is attributed to the assumptions made when defining material properties. In reality, the Young's modulus and Poisson's ratio are not constant throughout the FEM as it is assumed in the modeling of the thick-walled tube and arm simulations. Furthermore, venous walls, although thin, have different material composition than that of surrounding tissue and they also have heterogeneous mechanical properties. However, perhaps the most pronounced difference is the viscoelasticity, anisotropy and non-linear elasticity of tissues in the human arm whereas the simulations assumes that tissues are not viscoelastic and are homogeneous, isotropic and linearly elastic. Hence, future works will involve defining the mechanical properties of the arm more accurately and to translate such information for better finite element modeling.

For this experiment, the internal pressure in FEM is considered to be constant and pushing against the inner boundary in place of having a flow. Therefore, for more detailed representation of the real arm and accurate simulation of external loading on the arm model, co-simulation of the computational fluid dynamic model of blood flow along with FEM of the structure should be performed. For a computational fluid dynamic simulation, a section of a fluid is structured and meshed similar to the finite element model and the boundary condition will also include pressures at both ends. However, having a more accurate model will come at a cost of computational time.

$p_i$ (mmHg)	$E$ (kPa)	$\nu$	Calculated $\kappa_p$ (kPa)
7.5	47.5	0.45	$1.63 \times 10^7$
15	47.5	0.45	$1.63 \times 10^7$
22.5	47.5	0.45	$1.63 \times 10^7$
30	47.5	0.45	$1.63 \times 10^7$
37.5	47.5	0.45	$1.63 \times 10^7$

(A) Parameters used in FEM simulations

$p_i$ (mmHg)	$\kappa_p$ (kPa)	$n$	Calculated $E$ (kPa)
163.43	8.88	0.60	$2.59 \times 10^{-5}$
192.51	0.12	2.04	$3.36 \times 10^{-7}$
201.22	0.29	1.53	$8.56 \times 10^{-7}$
207.61	0.33	1.47	$9.58 \times 10^{-7}$
219.28	0.03	2.25	$9.40 \times 10^{-8}$

(B) Estimated Parameters using Curve Fitting

TABLE 6.1: A sample of comparison between the parameters used in the simulations and the estimated parameters by curve fitting using exponential model for the data in the post-buckling region

$p_i$ (mmHg)	$E$ (kPa)	$\nu$	Calculated $\kappa_p$ (kPa)
7.5	47.5	0.45	$1.63 \times 10^7$
15	47.5	0.45	$1.63 \times 10^7$
22.5	47.5	0.45	$1.63 \times 10^7$
30	47.5	0.45	$1.63 \times 10^7$
37.5	47.5	0.45	$1.63 \times 10^7$

(A) Parameters used in FEM simulations

$p_i$ (mmHg)	$\kappa_p$ (kPa)	$n$	Calculated $E$ (kPa)
1.61	309	0.274	$9.02 \times 10^{-4}$
1.70	291	0.282	$8.50 \times 10^{-4}$
1.81	280	0.286	$8.17 \times 10^{-4}$
1.83	260	0.296	$7.60 \times 10^{-4}$
1.83	246	0.303	$7.18 \times 10^{-4}$

(B) Estimated Parameters using Curve Fitting

TABLE 6.2: A sample of comparison between the parameters used in the simulations and the estimated parameters by curve fitting using modified exponential model for the data in the pre-buckling region

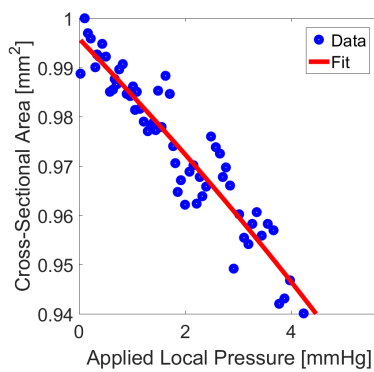
$p_i$ (mmHg)	$E$ (kPa)	$\nu$
7.5	40	0.45
15	40	0.45
22.5	40	0.45
30	40	0.45
37.5	40	0.45
7.5	47.5	0.45
15	47.5	0.45
22.5	47.5	0.45
30	47.5	0.45
37.5	47.5	0.45

(A) Parameters used in FEM simulations

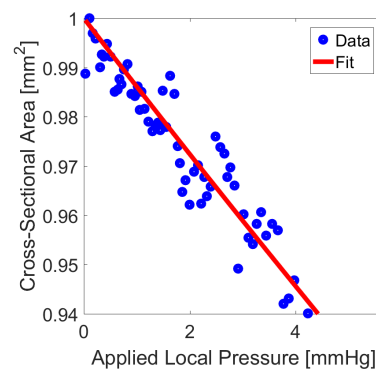
$p_i$ (mmHg)	$E$ (kPa)	$\nu$
7.12	38.44	0.448
13.96	36.69	0.446
20.04	35.35	0.444
25.32	33.62	0.442
30.19	31.89	0.440
6.98	46.24	0.449
14.42	44.62	0.447
20.37	42.98	0.445
25.91	41.11	0.443
31.70	39.80	0.442

(B) Estimated Parameters using Curve Fitting

TABLE 6.3: A sample of comparison between the parameters used in the simulations and the estimated parameters by curve fitting using quadratic model for the data in the small-strain region



(A) Exponential Model



(B) Modified Exponential Model

FIGURE 6.7: A sample of fitting on results from FEM simulation of a thick-walled tube using a quadratic model.

$p_i$ (mmHg)		
FEM	Exponential Model	Modified Exponential Model
7.5	$16.98 - i(1.55 \times 10^{-5})$	0.1665
15	$4.84 - i(2.80 \times 10^{-6})$	0.1174
22.5	$8.78 - i(1.10 \times 10^{-10})$	0.0111
30	$194.71 - i(2.60)$	0.3136
37.5	$-8.7704 - i(1.07 \times 10^{-5})$	0.0346

TABLE 6.4: A sample of comparison of internal pressures between one set by FEM and others estimated by different models

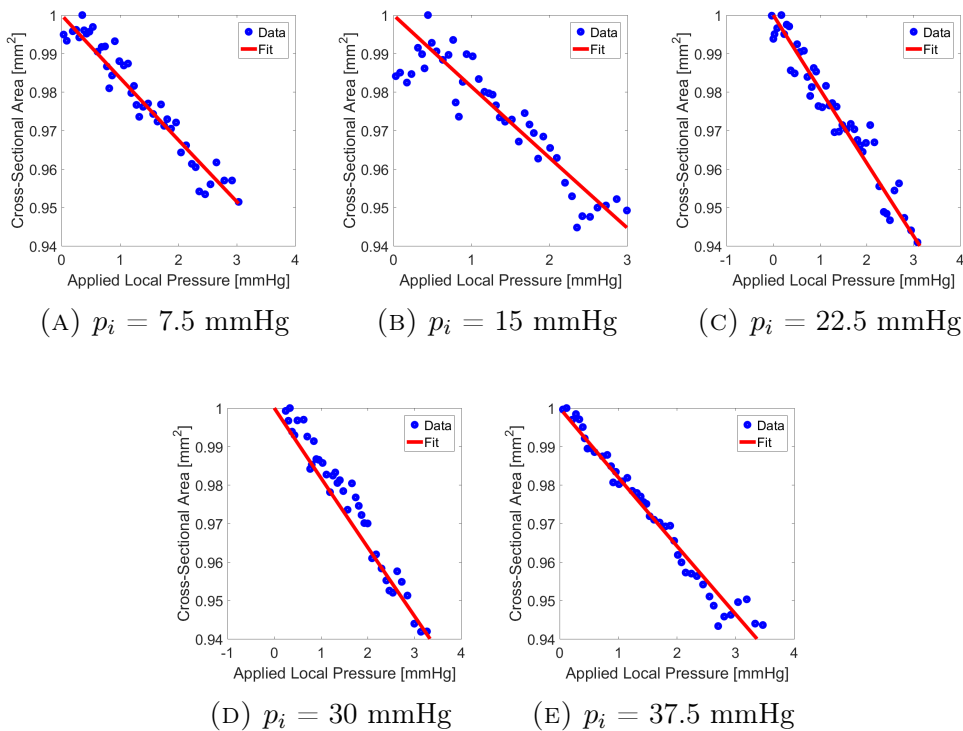


FIGURE 6.8: Data Fitting using Quadratic Model on a Small Strain Region with Young's modulus of 40 kPa

$p_i$ (mmHg)	$E$ (kPa)	$\nu$
7.5	40	0.45
15	40	0.45
22.5	40	0.45
30	40	0.45
37.5	40	0.45

(A) Parameters used in FEM simulations

$p_i$ (mmHg)	$E$ (kPa)	$\nu$
5.66	26.04	0.433
8.75	22.61	0.428
13.12	21.44	0.427
17.80	22.45	0.428
21.40	22.42	0.428

(B) Estimated Parameters using Curve Fitting

TABLE 6.5: A sample of comparison between the parameters used in the simulations and the estimated parameters by curve fitting using quadratic model for the data in the small-strain region

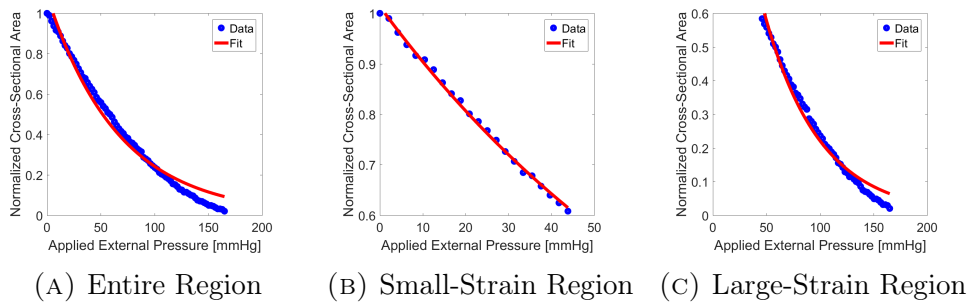


FIGURE 6.9: A sample of fitting on results from FEM simulation of a thick-walled tube using a modified exponential model.

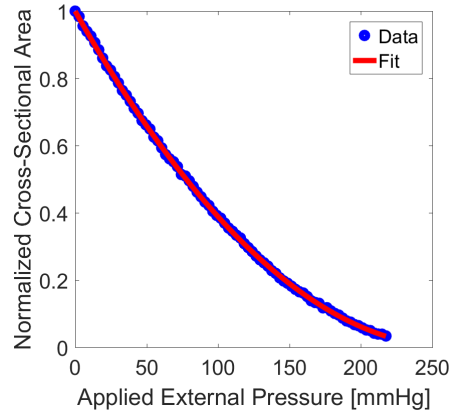


FIGURE 6.10: A sample of data fitting on the arm model using the quadratic model

$p_t$ (mmHg)	$E$ (kPa)	$\nu$
7.5	40	0.45
15	40	0.45
22.5	40	0.45
30	40	0.45
37.5	40	0.45
7.5	47.5	0.45
15	47.5	0.45
22.5	47.5	0.45
30	47.5	0.45
37.5	47.5	0.45
7.5	55	0.45
15	55	0.45
22.5	55	0.45
30	55	0.45
37.5	55	0.45

(A) Parameters used in FEM simulations

$p_t$ (mmHg)	$E$ (kPa)	$\nu$
8.01	41.00	0.451
15.79	41.57	0.451
23.72	42.48	0.452
30.95	43.00	0.453
38.32	43.66	0.453
7.00	47.66	0.450
16.08	48.96	0.451
23.71	49.89	0.452
34.20	58.91	0.461
38.55	51.39	0.454
8.23	55.79	0.451
16.08	56.36	0.452
26.66	61.75	0.458
33.51	63.59	0.460
38.56	57.81	0.453

(B) Estimated Parameters using Curve Fitting

TABLE 6.6: A comparison of parameters (A) set on FEM and (b) estimated using the quadratic model

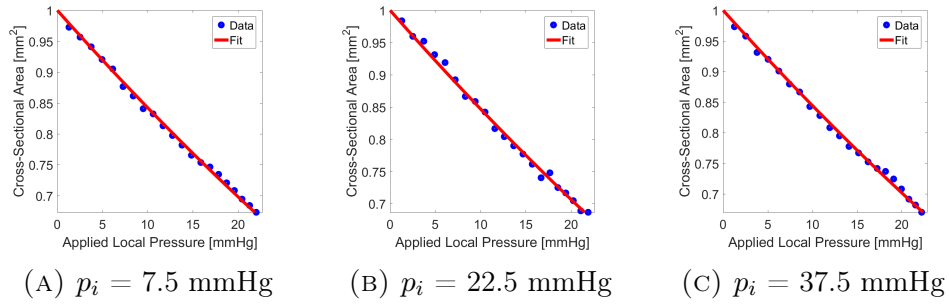


FIGURE 6.11: A sample of the goodness of the fit on results from FEM simulation of an arm model using a quadratic model.

$p_i$ (mmHg)	$E$ (kPa)	$\nu$
7.5	40	0.45
15	40	0.45
22.5	40	0.45
30	40	0.45
37.5	40	0.45
7.5	47.5	0.45
15	47.5	0.45
22.5	47.5	0.45
30	47.5	0.45
37.5	47.5	0.45
7.5	55	0.45
15	55	0.45
22.5	55	0.45
30	55	0.45
37.5	55	0.45

$p_i$ (mmHg)	$E$ (kPa)	$\nu$
4.16	16.762	0.421
6.73	16.739	0.421
10.33	17.376	0.422
13.75	17.475	0.422
16.77	17.412	0.422
3.95	19.499	0.421
6.57	18.719	0.420
10.58	21.032	0.422
13.59	20.429	0.422
16.56	20.183	0.421
3.07	21.295	0.419
6.66	23.204	0.421
10.42	22.856	0.421
13.05	23.244	0.421
16.27	23.174	0.421

(A) Parameters used in FEM simulations      (B) Estimated Parameters using Curve Fitting

TABLE 6.7: A comparison of parameters (A) set on FEM and (B) estimated using quadratic model

## Chapter 7

# General Discussion, Future Work and Conclusion

### 7.1 Discussion

The thesis aimed to introduce methods in estimating reperfusion rates in tissue microvasculature as well as estimating internal pressures of small vessels using photoacoustic-ultrasound dual imaging techniques. Both reperfusion rates and internal pressures of vessels are important parameters in assessing circulatory system and tissue health as an array of diseases can occur due to abnormal blood flow. Using the dual imaging technique allows the detection of blood in reference to the surrounding tissue structure, which allows localization of the abnormal vasculatures. By compressing on the tissue surface, the blood in the microvasculature is excluded and by measuring the applied load synchronously, the normalized area in respect to the applied pressure was measured. Furthermore, restoring the transducer to its original location allowed reperfusion that was represented by recovering photoacoustic signal. While the changes in signal strength were directly used for both assessment of internal pressure and reperfusion rates, we did not account for the changes in the absorption property of blood and soft tissue due to loading.

Photoacoustic monitoring of vessels during tissue compression was formulated as a means of estimating microvascular pressures, given the hypothesis

that vessel collapse would occur when external pressures overcome internal pressures. It was found that collapse points as measured by loss of photoacoustic signals were correlated with internal pressures, however, quantitative estimation was more challenging. Ex-vivo experiments demonstrated the correlation, but these experiments proved challenging owing to the size and fragility of vessel wall, undesired vessel collapse, clotting, etc. Finite element models were sought as a means of validation. We aimed to fit the relative changes in area as a function of compression to models for estimation of internal vascular pressures. Three analytical models were considered: Shapiro's exponential model, Shapiro's modified model, and a quadratic model. The quadratic model was newly proposed by our group. The Shapiro model was confirmed to be applicable only for thin-walled vessels, but inaccurate for vessels in thick tissue. Shapiro's modified model, which was also previously proposed by Shapiro himself, was found to provide a better fit for limited cases of vessels in thick tissue. The quadratic model was found to provide the best fitting results of the three models, but was valid only in limited situations such as small displacements in thick-walled tube and for the full compression in the arm model. All models were found to be inaccurate for top-loading situations, however, qualitative trends were achievable. This suggests that relative microvascular pressure imaging may still be possible.

Even relative pressure imaging could prove to have diagnostic value. Interestingly, our work suggests that pressure cuff measurements (based on vessel collapse and detection of Korotkoff sounds due to turbulence upon re-opening) may actually over-estimate internal pressures given that vessel buckling and pinching occurs at a much higher external pressure than the internal pressure. Clark et al., discuss systemic errors in cuff measurements relative to cuff size and compares them to other methods of measuring blood pressure [94]. While

---

factors such as cuff size were shown to impact pressure estimates, good concordance was found. This may suggest that our model may not yet fully account for realistic tissue mechanical properties. Otherwise our model predictions should provide a better match with sphygmomanometry. It should be noted that most of our simulations were for internal pressures less than 40mmHg, significantly lower than usually detected in the radial artery. Over-estimation of several mmHg may be less significant when measuring large pressures in the range of 80-120 mmHg. These over-estimates become more significant sources of relative error when measuring smaller pressures.

## 7.2 Future Work

While we successfully demonstrated label-free perfusion-rate imaging by estimating re-fill times after tissue compression, re-fill rates could depend on compressed tissue volume and may have complex depth dependence. Correlation with contrast-based perfusion imaging methods should be performed, although absolute concordance in perfusion rate values is not expected owing to different sizes of reperfusion volumes associated with different techniques. Nevertheless, even if estimated re-fill rates may be only semi-quantitative owing to these biases, our approach offers the first label-free subsurface method of perfusion-rate imaging to our knowledge. One potential application of this technology could be monitoring diabetic ulcers and peripheral vascular disease. Complications associated with these diseases represent billions of dollars in health care costs and early detection with suitable label-free screening methods could prevent such severe complications.

Future work on vessel pressure estimation should consider more realistic tissue models, accounting for strain-dependent visco-elastic properties and hyper-elastic properties. Additional work should also consider methods for calibrating for known overestimation. This could include using the compression technique

for vessels with known pressures from cuff-measurements or catheterization. It will require consultation with clinicians to determine how they would best use measurements of pressure in veins and microvascular networks. It represents a new technique which they have previously not had access to at all.

While the emphasis of this thesis has been on small vessels, the estimation techniques described here may also have applicability to large vessels. For example, an emerging trend is the periodic measurement of systemic blood pressure in high-risk patients using portable and wearable cuff systems. There could be marketable value in a potential system which could estimate internal vascular pressure without requiring such high pressures for vessel collapse.

### 7.3 Conclusion

The characterization and the assessment of hemodynamic through estimations of blood pressures of small vessels and reperfusion rates of a small volume of subsurface tissue using photoacoustic-ultrasound dual imaging technique has been introduced in this thesis. The setup required for both experiments is exactly identical with the blood pressure experiment focused on the compression by the imaging transducer while the reperfusion rate experiment is focused on the decompression of the transducer to restore tissue to its undeformed state. The estimation blood pressure of a non-arterial vessel *in vivo* using a mathematical model by Shapiro was further investigated by finite element simulation of an idealized human arm containing a single vein-like vessel. While results showed that estimation of blood pressure in relative to one another may be possible, the true quantification requires accurate knowledge of tissue mechanical properties. On the other hand, the validity of the estimation of reperfusion rates in subsurface region was proven as the change in reperfusion rate by varying the internal temperature of the hand was observed. Improvements could be made by studying the effects of compression area and the change in absorption

coefficient due to compression. Both techniques have potential to be applied in early detection of various vascular disease such as cancer.



# Bibliography

- [1] Rick A Nishimura et al. *2014 AHA / ACC Guideline for the Management of Patients With Valvular Heart Disease A Report of the American College of Cardiology / American Heart Association Task Force on Practice Guidelines*. Vol. 63. 22. 2014, pp. 2438–2488. ISBN: 0000000000000. DOI: [10.1161/CIR.0000000000000031/-/DC1](https://doi.org/10.1161/CIR.0000000000000031/-/DC1).. arXiv: [NIHMS150003](https://arxiv.org/abs/NIHMS150003).
- [2] William R. Hiatt et al. “Atherosclerotic peripheral vascular disease symposium II: Nomenclature for vascular diseases”. In: *Circulation* 118.25 (2008), pp. 2826–2829. ISSN: 00097322. DOI: [10.1161/CIRCULATIONAHA.108.191171](https://doi.org/10.1161/CIRCULATIONAHA.108.191171).
- [3] Dietmar W. Siemann. *The unique characteristics of tumor vasculature and preclinical evidence for its selective disruption by Tumor-Vascular Disrupting Agents*. 2011. DOI: [10.1016/j.ctrv.2010.05.001](https://doi.org/10.1016/j.ctrv.2010.05.001). arXiv: [NIHMS150003](https://arxiv.org/abs/NIHMS150003).
- [4] Surajit Bhattacharya and R.K. Mishra. “Pressure ulcers: Current understanding and newer modalities of treatment”. In: *Indian J Plast Surg* 48.1 (2015), pp. 4–16. ISSN: 0970-0358. DOI: [10.4103/0970](https://doi.org/10.4103/0970).
- [5] Kevin O’Rourke et al. “Cardiovascular Disease Worldwide, 1990-2013”. In: *Journal of American Medical Association* 314.18 (2015), p. 1905. DOI: [10.1001/jama.2015.8130.jama.com](https://doi.org/10.1001/jama.2015.8130.jama.com).
- [6] Ascher H. Shapiro. “Steady Flow in Collapsible Tubes”. In: 99.3 (1977), p. 126. ISSN: 01480731. DOI: [10.1115/1.3426281](https://doi.org/10.1115/1.3426281).

- [7] Timothy G. Foran and Noirin F. Sheahan. “Compression of the brachial artery in vivo”. In: *Physiological Measurement* 25.2 (2004), pp. 553–564. ISSN: 09673334. DOI: [10.1088/0967-3334/25/2/012](https://doi.org/10.1088/0967-3334/25/2/012).
- [8] Gary Drzewiecki et al. “Vessel growth and collapsible pressure-area relationship”. In: *American journal of physiology. Heart and circulatory physiology* 273 (2011), H2030–H2043.
- [9] “Perfusion MRI: The five most frequently asked technical questions”. In: 200.1 (2013), pp. 24–34. ISSN: 0361803X. DOI: [10.2214/AJR.12.9543](https://doi.org/10.2214/AJR.12.9543).
- [10] R Nakazato et al. “Myocardial perfusion imaging with PET.” In: *Imaging Med* 5.1 (2013), pp. 35–46. ISSN: 1755-5191. DOI: [10.2217/iim.13.1](https://doi.org/10.2217/iim.13.1). URL: <http://www.pubmedcentral.nih.gov/articlerender.fcgi?artid=3650901%7B%5C%7Dtool=pmcentrez%7B%5C%7Drendertype=abstract>.
- [11] A. A. Konstas et al. “Theoretic basis and technical implementations of CT perfusion in acute ischemic stroke, part 1: Theoretic basis”. In: 30.4 (2009), pp. 662–668. ISSN: 01956108. DOI: [10.3174/ajnr.A1487](https://doi.org/10.3174/ajnr.A1487).
- [12] David a Boas and Andrew K Dunn. “Laser speckle contrast imaging in biomedical optics.” In: *Journal of biomedical optics* 15.1 (2014), p. 011109. ISSN: 1560-2281. DOI: [10.1117/1.3285504](https://doi.org/10.1117/1.3285504).
- [13] Y-F Zhou. “High intensity focused ultrasound in clinical tumor ablation”. In: *World J. Clin. Oncol.* 2.1 (2011), pp. 8–27. DOI: [10.5306/wjco.v2.i1.TOPIC](https://doi.org/10.5306/wjco.v2.i1.TOPIC).
- [14] Jean-Claude Pineau et al. “Body Fat Mass Assessment: A Comparison between an Ultrasound-Based Device and a Discovery A Model of DXA”. In: *ISRN Obesity* 2013 (2013), pp. 1–5. ISSN: 2090-9446. DOI: [10.1155/2013/462394](https://doi.org/10.1155/2013/462394). URL: <http://www.hindawi.com/journals/isrn/2013/462394/>.

- [15] Ayumi Ido et al. “Ultrasound-derived abdominal muscle thickness better detects metabolic syndrome risk in obese patients than skeletal muscle index measured by dual-energy X-ray absorptiometry”. In: *PLoS ONE* 10.12 (2015). ISSN: 19326203. DOI: [10.1371/journal.pone.0143858](https://doi.org/10.1371/journal.pone.0143858).
- [16] Giampiero I. Baroncelli. “Quantitative ultrasound methods to assess bone mineral status in children: Technical characteristics, performance, and clinical application”. In: 63.3 (2008), pp. 220–228. ISSN: 00313998. DOI: [10.1203/PDR.0b013e318163a286](https://doi.org/10.1203/PDR.0b013e318163a286).
- [17] Nandan S. Anavekar and Jae K. Oh. “Doppler echocardiography: A contemporary review”. In: *Journal of Cardiology* 54.3 (2009), pp. 347–358. ISSN: 09145087. DOI: [10.1016/j.jjcc.2009.10.001](https://doi.org/10.1016/j.jjcc.2009.10.001).
- [18] David E. Goertz et al. “High-frequency Doppler ultrasound monitors the effects of antivascular therapy on tumor blood flow”. In: *Cancer Research* 62.22 (2002), pp. 6371–6375. ISSN: 00085472.
- [19] Stephanie C. Wu et al. *Foot ulcers in the diabetic patient, prevention and treatment*. 2007. DOI: [10.3310/hta13540](https://doi.org/10.3310/hta13540).
- [20] Luciana P. Fernandes Abbade and Sidnei Lastória. *Venous ulcer: Epidemiology, physiopathology, diagnosis and treatment*. 2005. DOI: [10.1111/j.1365-4632.2004.02456.x](https://doi.org/10.1111/j.1365-4632.2004.02456.x).
- [21] J M Rubin et al. “Power Doppler US: a potentially useful alternative to mean frequency-based color Doppler US.” In: *Radiology* 190.3 (1994), pp. 853–856. ISSN: 0033-8419. DOI: [10.1148/radiology.190.3.8115639](https://doi.org/10.1148/radiology.190.3.8115639). URL: <http://pubs.rsna.org/doi/10.1148/radiology.190.3.8115639>.
- [22] Mesut Remzi et al. “Can power doppler enhanced transrectal ultrasound guided biopsy improve prostate cancer detection on first and repeat prostate

- biopsy?” In: *European Urology* 46.4 (2004), pp. 451–456. ISSN: 03022838. DOI: [10.1016/j.eururo.2004.06.002](https://doi.org/10.1016/j.eururo.2004.06.002).
- [23] Carlo A. Sciré et al. “Ultrasonographic evaluation of joint involvement in early rheumatoid arthritis in clinical remission: Power Doppler signal predicts short-term relapse”. In: *Rheumatology* 48.9 (2009), pp. 1092–1097. ISSN: 14620324. DOI: [10.1093/rheumatology/kep171](https://doi.org/10.1093/rheumatology/kep171).
- [24] Cornelis D. de Kroon et al. “Power doppler area in the diagnosis of endometrial cancer”. In: *International Journal of Gynecological Cancer* 20.7 (2010), p. 1. ISSN: 15251438. DOI: [10.1111/IGC.0b013e3181f0df98](https://doi.org/10.1111/IGC.0b013e3181f0df98).
- [25] Mariusz Dubiel et al. “Fetal and placental power Doppler imaging in normal and high-risk pregnancy”. In: *European Journal of Ultrasound* 9.3 (1999), pp. 223–230. ISSN: 09298266. DOI: [10.1016/S0929-8266\(99\)00027-0](https://doi.org/10.1016/S0929-8266(99)00027-0).
- [26] R. Cruz-Martinez et al. “Normal reference ranges of fetal regional cerebral blood perfusion as measured by fractional moving blood volume”. In: *Ultrasound in Obstetrics and Gynecology* 37.2 (2011), pp. 196–201. ISSN: 09607692. DOI: [10.1002/uog.7722](https://doi.org/10.1002/uog.7722).
- [27] G N Stevenson et al. “A technique for the estimation of fractional moving blood volume by using three-dimensional power doppler US”. In: *Radiology* 274.1 (2015), pp. 230–237. ISSN: 00338419 (ISSN). DOI: [10.1148/radiol.14132363](https://doi.org/10.1148/radiol.14132363). URL: <https://www.scopus.com/inward/record.uri?eid=2-s2.0-84919724049%7B%5C%7DpartnerID=40%7B%5C%7Dmd5=9da42d7c5cc06906c0a6bbea2ca3c5e7>.
- [28] Vera Paefgen, Dennis Doleschel, and Fabian Kiessling. “Evolution of contrast agents for ultrasound imaging and ultrasound-mediated drug delivery”. In: *Frontiers in Pharmacology* 6.SEP (2015), pp. 1–16. ISSN: 16639812. DOI: [10.3389/fphar.2015.00197](https://doi.org/10.3389/fphar.2015.00197).

- [29] C. F. Dietrich et al. “An EFSUMB introduction into dynamic contrast-enhanced ultrasound (DCE-US) for quantification of tumour perfusion”. In: *Ultraschall in der Medizin* 33.4 (2012), pp. 344–351. ISSN: 01724614. DOI: [10.1055/s-0032-1313026](https://doi.org/10.1055/s-0032-1313026).
- [30] Kathryn R Nightingale et al. “Acoustic radiation force impulse imaging: in vivo demonstration of clinical feasibility.” In: *Ultrasound Med Biol* 28.2 (2002), pp. 227–235. ISSN: 0301-5629. DOI: [10.1016/S0301-5629\(01\)00499-9](https://doi.org/10.1016/S0301-5629(01)00499-9).
- [31] J. L. Gennisson et al. “Ultrasound elastography: Principles and techniques”. In: *Diagnostic and Interventional Imaging* 94.5 (2013), pp. 487–495. ISSN: 22115706. DOI: [10.1016/j.diii.2013.01.022](https://doi.org/10.1016/j.diii.2013.01.022). URL: <http://dx.doi.org/10.1016/j.diii.2013.01.022>.
- [32] J Ophir et al. “Elastography: a quantitative method for imaging the elasticity of biological tissues.” In: *Ultrasonic imaging* 13.2 (1991), pp. 111–134. ISSN: 01617346. DOI: [10.1016/0161-7346\(91\)90079-W](https://doi.org/10.1016/0161-7346(91)90079-W).
- [33] Tomy Varghese. “Quasi-Static Ultrasound Elastography”. In: *Ultrasound Clinics* 4.3 (2009), pp. 323–338. ISSN: 1556858X. DOI: [10.1016/j.cult.2009.10.009](https://doi.org/10.1016/j.cult.2009.10.009). URL: <http://dx.doi.org/10.1016/j.cult.2009.10.009>.
- [34] Lihong V. Wang and Hsin-I Wu. *Biomedical Optics: Principles and Imaging*. 2012. ISBN: 9780471743040. DOI: [10.1002/9780470177013](https://doi.org/10.1002/9780470177013). arXiv: [arXiv:1011.1669v3](https://arxiv.org/abs/1011.1669v3).
- [35] Minghua Xu and Lihong V. Wang. “Photoacoustic imaging in biomedicine”. In: *Review of Scientific Instruments* 77.4 (2006), pp. 1–22. ISSN: 00346748. DOI: [10.1063/1.2195024](https://doi.org/10.1063/1.2195024).

- [36] Jun Xia, Junjie Yao, and Lihong V Wang. “Photoacoustic tomography: principles and advances”. In: *Electromagn Waves (Camb)* 147 (2014), pp. 1–22. ISSN: 0022-1724. DOI: [10.1016/j.biotechadv.2011.08.021](https://doi.org/10.1016/j.biotechadv.2011.08.021). Secreted. arXiv: NIHMS150003. URL: <http://www.ncbi.nlm.nih.gov/pubmed/25642127%7B%5C%7D5Cnhttp://www.pubmedcentral.nih.gov/articlerender.fcgi?artid=PMC4311576%7B%5C%7D5Cnhttp://www.ncbi.nlm.nih.gov/pubmed/25642127%7B%5C%7D5Cnhttp://www.ncbi.nlm.nih.gov/pmc/articles/PMC4311576/pdf/nihms610461.pdf>.
- [37] Srirang Manohar and Daniel Razansky. “Photoacoustics : a historical review”. In: *Advances in Optics and Photonics* 8.4 (2016), pp. 586–617. ISSN: 1943-8206. DOI: [10.1364/AOP.8.000586](https://doi.org/10.1364/AOP.8.000586).
- [38] “Photoacoustic doppler effect from flowing small light-absorbing particles”. In: *Physical Review Letters* 99.18 (2007). ISSN: 00319007. DOI: [10.1103/PhysRevLett.99.184501](https://doi.org/10.1103/PhysRevLett.99.184501).
- [39] Joanna Bruncker and Paul Beard. “Pulsed photoacoustic Doppler flowmetry using time-domain cross-correlation: Accuracy, resolution and scalability”. In: *The Journal of the Acoustical Society of America* 132.3 (2012), pp. 1780–1791. ISSN: 0001-4966. DOI: [10.1121/1.4739458](https://doi.org/10.1121/1.4739458). URL: <http://asa.scitation.org/doi/10.1121/1.4739458>.
- [40] Joanna Bruncker and Paul Beard. “Velocity measurements in whole blood using acoustic resolution photoacoustic Doppler”. In: *Biomedical optics express* 7.7 (2016), pp. 2789–2806. ISSN: 16057422. DOI: [10.1364/BOE.7.002789](https://doi.org/10.1364/BOE.7.002789).
- [41] Lun-De Liao et al. “Imaging brain hemodynamic changes during rat forepaw electrical stimulation using functional photoacoustic microscopy”. In: *NeuroImage* 52.2 (2010), pp. 562–570. ISSN: 10538119. DOI: [10.1016/j](https://doi.org/10.1016/j).

- neuroimage.2010.03.065. URL: <http://linkinghub.elsevier.com/retrieve/pii/S1053811910003526>.
- [42] Joon-Mo Yang et al. “Simultaneous functional photoacoustic and ultrasonic endoscopy of internal organs in vivo”. In: *Nature Medicine* 18.8 (2012), pp. 1297–1302. ISSN: 1078-8956. DOI: [10.1038/nm.2823](https://doi.org/10.1038/nm.2823). arXiv: NIHMS150003. URL: <http://www.nature.com/doifinder/10.1038/nm.2823>.
- [43] Hao F Zhang et al. “Functional photoacoustic microscopy for high-resolution and noninvasive in vivo imaging”. In: *Nature Biotechnology* 24.7 (2006), pp. 848–851. ISSN: 1087-0156. DOI: [10.1038/nbt1220](https://doi.org/10.1038/nbt1220). URL: <http://www.nature.com/doifinder/10.1038/nbt1220>.
- [44] John Allen and Kevin Howell. “Microvascular imaging: techniques and opportunities for clinical physiological measurements”. In: *Physiological Measurement* 35.7 (2014), R91–R141. ISSN: 0967-3334. DOI: [10.1088/0967-3334/35/7/R91](https://doi.org/10.1088/0967-3334/35/7/R91). URL: <http://stacks.iop.org/0967-3334/35/i=7/a=R91?key=crossref.ee8e71d4b5b7e4e81d7b47c95a790118>.
- [45] C. Chad Quarles et al. “Comparison of dual-echo DSC-MRI- and DCE-MRI-derived contrast agent kinetic parameters”. In: *Magnetic Resonance Imaging* 30.7 (2012), pp. 944–953. ISSN: 0730725X. DOI: [10.1016/j.mri.2012.03.008](https://doi.org/10.1016/j.mri.2012.03.008). arXiv: NIHMS150003.
- [46] Yvonne W. Lui et al. “Evaluation of CT perfusion in the setting of cerebral ischemia: Patterns and pitfalls”. In: 31.9 (2010), pp. 1552–1563. ISSN: 01956108. DOI: [10.3174/ajnr.A2026](https://doi.org/10.3174/ajnr.A2026).
- [47] “Imaging of stroke: Part 1, perfusion CT - Overview of imaging technique, interpretation pearls, and common pitfalls”. In: 198.1 (2012), pp. 52–62. ISSN: 0361803X. DOI: [10.2214/AJR.10.7255](https://doi.org/10.2214/AJR.10.7255).

- [48] M. F. Di Carli et al. “Clinical Myocardial Perfusion PET/CT”. In: *Journal of Nuclear Medicine* 48.5 (2007), pp. 783–793. ISSN: 0161-5505. DOI: [10.2967/jnumed.106.032789](https://doi.org/10.2967/jnumed.106.032789). URL: <http://jnm.snmjournals.org/cgi/doi/10.2967/jnumed.106.032789>.
- [49] *Review of laser speckle contrast techniques for visualizing tissue perfusion*. 2009. DOI: [10.1007/s10103-008-0626-3](https://doi.org/10.1007/s10103-008-0626-3).
- [50] Daniel De Backer et al. “Monitoring the microcirculation in the critically ill patient: current methods and future approaches.” In: *Intensive care medicine* 36.11 (2010), pp. 1813–25. ISSN: 1432-1238. DOI: [10.1007/s00134-010-2005-3](https://doi.org/10.1007/s00134-010-2005-3). URL: <http://www.ncbi.nlm.nih.gov/pubmed/20689916>.
- [51] Maurizio Cutolo and M. Matucci Cerinic. “Nailfold capillaroscopy and classification criteria for systemic sclerosis”. In: *Clinical and Experimental Rheumatology* 25.5 (2007), pp. 663–665. ISSN: 0392856X. DOI: [10.3899/jrheum.131284](https://doi.org/10.3899/jrheum.131284).
- [52] Marek M. Chojnowski, Anna Felis-Giemza, and Olesińska. *Capillaroscopy - A role in modern rheumatology*. 2016. DOI: [10.5114/reum.2016.60215](https://doi.org/10.5114/reum.2016.60215).
- [53] T. W L Scheeren, P. Schober, and L. A. Schwarte. “Monitoring tissue oxygenation by near infrared spectroscopy (NIRS): Background and current applications”. In: *Journal of Clinical Monitoring and Computing* 26.4 (2012), pp. 279–287. ISSN: 13871307. DOI: [10.1007/s10877-012-9348-y](https://doi.org/10.1007/s10877-012-9348-y).
- [54] Theodore A Henderson and Larry D Morries. “Near-infrared photonic energy penetration: can infrared phototherapy effectively reach the human brain?” In: *Neuropsychiatric disease and treatment* 11 (2015), pp. 2191–208. ISSN: 1176-6328. DOI: [10.2147/NDT.S78182](https://doi.org/10.2147/NDT.S78182). URL: <http://www.pubmedcentral.nih.gov/articlerender.fcgi?artid=4552256%7B%5C%7Dtool=pmcentrez%7B%5C%7Drendertype=abstract>.

- [55] Michael B. Wallace et al. *Reflectance Spectroscopy*. 2009. DOI: [10.1016/j.giec.2009.02.008](https://doi.org/10.1016/j.giec.2009.02.008).
- [56] Joseph E. Flaherty, Joseph B. Keller, and S. I. Rubinow. “Post Buckling Behavior of Elastic Tubes and Rings with Opposite Sides in Contact”. In: *SIAM Journal on Applied Mathematics* 23.4 (1972), pp. 446–455. ISSN: 0036-1399. DOI: [10.1137/0123047](https://doi.org/10.1137/0123047). URL: <http://epubs.siam.org/doi/abs/10.1137/0123047>.
- [57] Shinsaku Tsuji et al. “Analysis of ischemia-reperfusion injury in a microcirculatory model of pressure ulcers”. In: *The International Journal of Tissue Repair and Regeneration* (2005), pp. 209–215.
- [58] Anatole Harrois, Laurent Dupic, and Jacques Duranteau. “Targeting the microcirculation in resuscitation of acutely unwell patients.” In: *Current opinion in critical care* 17.3 (2011), pp. 303–7. ISSN: 1531-7072. DOI: [10.1097/MCC.0b013e3283466ba0](https://doi.org/10.1097/MCC.0b013e3283466ba0). URL: <http://www.ncbi.nlm.nih.gov/pubmed/21499095>.
- [59] Namkje a R Vellinga et al. “Study Design of the Microcirculatory Shock Occurrence in Acutely Ill Patients (microSOAP): an International Multicenter Observational Study of Sublingual Microcirculatory Alterations in Intensive Care Patients”. In: *Critical care research and practice* 2012 (2012), pp. 1–7. ISSN: 2090-1313. DOI: [10.1155/2012/121752](https://doi.org/10.1155/2012/121752). URL: <http://www.hindawi.com/journals/ccrp/2012/121752/%7B%5C%7D5Cnhttp://www.pubmedcentral.nih.gov/articlerender.fcgi?artid=3359769%7B%5C%7Dtool=pmcentrez%7B%5C%7Drendertype=abstract>.
- [60] R. Phillip Dellinger et al. “Surviving Sepsis Campaign: International guidelines for management of severe sepsis and septic shock: 2008”. In: *Intensive Care Medicine* 34.1 (2008), pp. 17–60. ISSN: 0342-4642. DOI: [10.1007/](https://doi.org/10.1007/)

- s00134-007-0934-2. URL: <http://link.springer.com/10.1007/s00134-007-0934-2>.
- [61] Vladimir Cerny. “Sublingual microcirculation”. In: *Applied Cardiopulmonary Pathophysiology* (2012). ISSN: 09205268.
- [62] “Biophysical aspects of blood flow in the microvasculature”. In: *Cardiovascular Research* 32.4 (1996), pp. 654–667. ISSN: 00086363. DOI: [10.1016/0008-6363\(96\)00065-X](https://doi.org/10.1016/0008-6363(96)00065-X).
- [63] Hai-Chao Han et al. “Artery Buckling: New Phenotypes, Models, and Applications”. In: *Annals of Biomedical Engineering* 41.7 (2013), pp. 1399–1410. ISSN: 0090-6964. DOI: [10.1007/s10439-012-0707-0](https://doi.org/10.1007/s10439-012-0707-0). arXiv: NIHMS150003. URL: <http://link.springer.com/10.1007/s10439-012-0707-0>.
- [64] P G Pavan et al. “Constitutive Modeling of Time-Dependent Response of Human Plantar Aponeurosis”. In: *Computational and Mathematical Methods in Medicine* 2014 (2014). DOI: <http://dx.doi.org/10.1155/2014/530242>.
- [65] Hassan Rivaz et al. “Real-time regularized ultrasound elastography”. In: *IEEE Transactions on Medical Imaging* 30.4 (2011), pp. 928–945. ISSN: 02780062. DOI: [10.1109/TMI.2010.2091966](https://doi.org/10.1109/TMI.2010.2091966).
- [66] “Severe sepsis and septic shock: Clinical overview and update on management”. In: *Mayo Clinic Proceedings* 89.11 (2014), pp. 1572–1578. ISSN: 19425546. DOI: [10.1016/j.mayocp.2014.07.009](https://doi.org/10.1016/j.mayocp.2014.07.009). URL: <http://dx.doi.org/10.1016/j.mayocp.2014.07.009>.
- [67] Jill Cox. “Predictors of Pressure Ulcers in Adult Critical Care Patients”. In: *American Journal of Critical Care* 20.5 (2011), pp. 364–375.

- [68] Asami Satoh et al. “Role of Perfusion CT in Assessing Tumor Blood Flow and Malignancy Level of Gastric Cancer”. In: *Digestive Surgery* 27.4 (2010), pp. 253–260. ISSN: 02534886. DOI: [10.1159/000288703](https://doi.org/10.1159/000288703).
- [69] Giovanna Russo et al. “Angiogenesis in prostate cancer: Onset, progression and imaging”. In: *BJU International* 110.11 C (2012), pp. 794–808. ISSN: 14644096. DOI: [10.1111/j.1464-410X.2012.11444.x](https://doi.org/10.1111/j.1464-410X.2012.11444.x).
- [70] M H Gorelick, K N Shaw, and M D Baker. *Effect of ambient temperature on capillary refill in healthy children*. Tech. rep. 5. 1993, pp. 699–702.
- [71] Anna-Theresa Lobos and Kusum Menon. “A multidisciplinary survey on capillary refill time: Inconsistent performance and interpretation of a common clinical test.” In: *Pediatric critical care medicine : a journal of the Society of Critical Care Medicine and the World Federation of Pediatric Intensive and Critical Care Societies* 9.4 (2008), pp. 386–91. DOI: [10.1097/PCC.0b013e3181728798](https://doi.org/10.1097/PCC.0b013e3181728798).
- [72] Amelia Pickard, Walter Karlen, and J. Mark Ansermino. “Capillary refill time: Is it still a useful clinical sign?” In: *Anesthesia and Analgesia* 113.1 (2011), pp. 120–123. ISSN: 00032999. DOI: [10.1213/ANE.0b013e31821569f9](https://doi.org/10.1213/ANE.0b013e31821569f9).
- [73] Bronwyn Anderson et al. “Impact of patient and environmental factors on capillary refill time in adults”. In: *American Journal of Emergency Medicine* 26.1 (2008), pp. 62–65. ISSN: 07356757. DOI: [10.1016/j.ajem.2007.06.026](https://doi.org/10.1016/j.ajem.2007.06.026).
- [74] Rajan V;Varghese B;Van Leeuwen TG;Steenbergen W. “Influence of tissue optical properties on laser Doppler perfusion imaging,accounting for photon penetration depth and the laser speckle phenomenon.” In: *J Biomed Opt* 13.2 (2008), p. 24001. ISSN: 1083-3668/1083-3668.

- [75] A. Humeau-Heurtier et al. “Relevance of laser doppler and laser speckle techniques for assessing vascular function: State of the art and future trends”. In: *IEEE Transactions on Biomedical Engineering* 60.3 (2013), pp. 659–666. ISSN: 00189294. DOI: [10.1109/TBME.2013.2243449](https://doi.org/10.1109/TBME.2013.2243449).
- [76] Jonathan R. Lindner et al. “Limb Stress-Rest Perfusion Imaging With Contrast Ultrasound for the Assessment of Peripheral Arterial Disease Severity”. In: *JACC: Cardiovascular Imaging* 1.3 (2008), pp. 343–350. ISSN: 1936878X. DOI: [10.1016/j.jcmg.2008.04.001](https://doi.org/10.1016/j.jcmg.2008.04.001).
- [77] David Cosgrove and Nathalie Lassau. “Imaging of perfusion using ultrasound.” In: *European journal of nuclear medicine and molecular imaging* 37 Suppl 1. July (Aug. 2010), S65–85. ISSN: 1619-7089. DOI: [10.1007/s00259-010-1537-7](https://doi.org/10.1007/s00259-010-1537-7). URL: <http://www.ncbi.nlm.nih.gov/pubmed/20640418>.
- [78] F Kiessling, J Huppert, and M Palmowski. “Functional and molecular ultrasound imaging: concepts and contrast agents.” In: *Current medicinal chemistry* 16.5 (2009), pp. 627–642. ISSN: 09298673. DOI: [10.2174/092986709787458470](https://doi.org/10.2174/092986709787458470).
- [79] Daniel Duerschmied et al. “Contrast ultrasound perfusion imaging of lower extremities in peripheral arterial disease: A novel diagnostic method”. In: *European Heart Journal* 27.3 (2006), pp. 310–315. ISSN: 0195668X. DOI: [10.1093/eurheartj/ehi636](https://doi.org/10.1093/eurheartj/ehi636).
- [80] Taniyel Ay et al. “Destruction of contrast microbubbles by ultrasound: effects on myocardial function, coronary perfusion pressure, and microvascular integrity.” In: *Circulation* 104.4 (2001), pp. 461–466. ISSN: 0009-7322. DOI: [10.1161/hc3001.092038](https://doi.org/10.1161/hc3001.092038).
- [81] Jeane M Tsutsui, Feng Xie, and Richard Thomas Porter. “The use of microbubbles to target drug delivery.” In: *Cardiovascular ultrasound* 2

- (2004), p. 23. ISSN: 1476-7120. DOI: [10.1186/1476-7120-2-23](https://doi.org/10.1186/1476-7120-2-23). eprint: [NIHMS150003](https://pubmed.ncbi.nlm.nih.gov/150003/).
- [82] “Models and methods for analyzing DCE-MRI: A review”. In: *Medical Physics* 41.12 (2014), p. 124301. ISSN: 0094-2405. DOI: [10.1118/1.4898202](https://doi.org/10.1118/1.4898202). URL: <http://scitation.aip.org/content/aapm/journal/medphys/41/12/10.1118/1.4898202>.
- [83] T. S. Koh et al. “Cerebral perfusion mapping using a robust and efficient method for deconvolution analysis of dynamic contrast-enhanced images”. In: *NeuroImage* 32.2 (2006), pp. 643–653. ISSN: 10538119. DOI: [10.1016/j.neuroimage.2006.03.042](https://doi.org/10.1016/j.neuroimage.2006.03.042).
- [84] Joël J. Niederhauser et al. “Combined ultrasound and optoacoustic system for real-time high-contrast vascular imaging in vivo”. In: *IEEE Transactions on Medical Imaging* 24.4 (2005), pp. 436–440. ISSN: 02780062. DOI: [10.1109/TMI.2004.843199](https://doi.org/10.1109/TMI.2004.843199).
- [85] Song Hu and Lihong V Wang. “Photoacoustic imaging and characterization of the microvasculature.” In: *Journal of biomedical optics* 15.1 (2010), p. 011101. ISSN: 1560-2281. DOI: [10.1117/1.3281673](https://doi.org/10.1117/1.3281673). URL: <http://www.pubmedcentral.nih.gov/articlerender.fcgi?artid=2821418%7B%5C%7Dtool=pmcentrez%7B%5C%7Drendertype=abstract>.
- [86] Junjie Yao. “Transverse flow imaging based on photoacoustic Doppler bandwidth broadening”. In: *Journal of Biomedical Optics* 15.2 (2010), p. 021304. ISSN: 1083-3668. DOI: [10.1117/1.3339953](https://doi.org/10.1117/1.3339953). URL: <http://biomedicaloptics.spiedigitallibrary.org/article.aspx?doi=10.1117/1.3339953>.
- [87] H. Rivaz et al. “Ultrasound elastography: A dynamic programming approach”. In: *IEEE Transactions on Medical Imaging* 27.10 (2008), pp. 1373–1377. ISSN: 0278-0062. DOI: [10.1109/TMI.2008.917243](https://doi.org/10.1109/TMI.2008.917243).

- [88] E. K Chan et al. “Effects of compression on soft tissue optical properties”. In: *IEEE Journal of Selected Topics in Quantum Electronics* 2.4 (1996), pp. 943–950. ISSN: 1077-260X. DOI: [10.1109/2944.577320](https://doi.org/10.1109/2944.577320). URL: <http://ieeexplore.ieee.org/ielx1/2944/12536/00577320.pdf?tp=%7B%5C%7Darnumber=577320%7B%5C%7Disnumber=12536>.
- [89] A. Tirella, G. Mattei, and A. Ahluwalia. “Strain rate viscoelastic analysis of soft and highly hydrated biomaterials”. In: *Journal of Biomedical Materials Research - Part A* 102.10 (2014), pp. 3352–3360. ISSN: 15524965. DOI: [10.1002/jbm.a.34914](https://doi.org/10.1002/jbm.a.34914).
- [90] Javier Palacio-Torralla et al. “Quantitative diagnostics of soft tissue through viscoelastic characterization using time-based instrumented palpation”. In: *Journal of the Mechanical Behavior of Biomedical Materials* 41 (2015), pp. 149–160. ISSN: 18780180. DOI: [10.1016/j.jmbbm.2014.09.027](https://doi.org/10.1016/j.jmbbm.2014.09.027). URL: <http://dx.doi.org/10.1016/j.jmbbm.2014.09.027>.
- [91] HongMei Zhang, Yue Wang, and Michael F Insana. “Ramp-hold relaxation solutions for the KVFD model applied to soft viscoelastic media”. In: *Measurement Science and Technology* 27.2 (2016), p. 025702. ISSN: 0957-0233. DOI: [10.1088/0957-0233/27/2/025702](https://doi.org/10.1088/0957-0233/27/2/025702). URL: <http://stacks.iop.org/0957-0233/27/i=2/a=025702?key=crossref.bb3536a42f53702f89b51c9b5b34b374>.
- [92] Rinaldo Vallascas and Mariangela Usai. “New FEM 3D model for arm-cuff interface simulation”. In: *2015 IEEE International Symposium on Medical Measurements and Applications, MeMeA 2015 - Proceedings* (2015), pp. 445–450. DOI: [10.1109/MeMeA.2015.7145245](https://doi.org/10.1109/MeMeA.2015.7145245).
- [93] H. Lan et al. “Effect of tissue mechanical properties on cuff-based blood pressure measurements”. In: *Medical Engineering & Physics* 33.10 (2011), pp. 1287–1292. ISSN: 13504533. DOI: [10.1016/j.medengphy.2011](https://doi.org/10.1016/j.medengphy.2011).

- 06.006. URL: <http://linkinghub.elsevier.com/retrieve/pii/S1350453311001433>.
- [94] J A Clark et al. “Discrepancies between direct and indirect blood pressure measurements using various recommendations for arm cuff selection”. In: *Pediatrics* 110.5 (2002), pp. 920–923. ISSN: 1098-4275. DOI: [10.1542/peds.110.5.920](https://doi.org/10.1542/peds.110.5.920).
- [95] Allan F. Bower. *Applied Mechanics of Solids*. 2009, p. 820. ISBN: 978-1-4398-0247-2.



## Appendix A

# Derivation of The Quadratic Model

Some of the equations, boundary conditions and assumptions for approximations required for the following derivation has been obtained from Chapter 4 of '*Applied Mechanics of Solids*' by Bower [95].

For a linearly elastic isotropic solid with a known geometry, constitutive law for the material, boundary tractions and displacements including an assumption that all displacements are small, displacement, strain and stress fields, denoted as  $u_i$ ,  $\epsilon_{ij}$  and  $\sigma_{ij}$ , respectively, are related by the following set of equations :

$$\epsilon_{ij} = \frac{1}{2} \left( \frac{\partial u_i}{\partial x_j} + \frac{\partial u_j}{\partial x_i} \right) \quad (\text{A.1})$$

$$\sigma_{ij} = \frac{E}{1 + \nu} \left( \epsilon_{ij} + \frac{\nu}{1 - 2\nu} \epsilon_{kk} \delta_{ij} \right) - \frac{E\alpha\Delta T}{1 - 2\nu} \delta_{ij} \quad (\text{A.2})$$

$$\frac{\partial \sigma_{ij}}{\partial x_i} + \rho_0 b_j = \rho_0 \vec{a}_j \quad (\text{A.3})$$

where  $E$  is Young's modulus,  $\nu$  is Poisson's ratio,  $\rho_0$  is the mass density  $\vec{a}$  is the acceleration of a point on the material and  $\Delta T$  is the temperature distribution in the solid. These three equations are termed displacement-strain equation, stress-strain equation and equilibrium equation, respectively.

For an axially symmetric cylinder, each location can be defined by a cylindrical coordinate system  $(r, \theta, z)$  and vectors can be defined using basis components  $(\vec{e}_r, \vec{e}_\theta, \vec{e}_z)$ . Therefore, position, displacement, body force and acceleration

vector can be respectively written in the following forms:

$$\vec{x} = r\vec{e}_r + z\vec{e}_z \quad (\text{A.4})$$

$$\vec{u} = u(r)\vec{e}_r + \epsilon_{zz}z\vec{e}_z \quad (\text{A.5})$$

$$\vec{b} = \rho_0 b(r)\vec{e}_r \quad (\text{A.6})$$

$$\vec{a} = -\omega^2 r\vec{e}_r \quad (\text{A.7})$$

and the stress and strain tensors can be written as follows:

$$\sigma = \begin{bmatrix} \sigma_{rr} & 0 & 0 \\ 0 & \sigma_{\theta\theta} & 0 \\ 0 & 0 & \sigma_{zz} \end{bmatrix} \quad \epsilon = \begin{bmatrix} \epsilon_{rr} & 0 & 0 \\ 0 & \epsilon_{\theta\theta} & 0 \\ 0 & 0 & \epsilon_{zz} \end{bmatrix} \quad (\text{A.8})$$

Substituting equation A.8 into A.1, A.2 and A.3 show yields :

$$\epsilon_{rr} = \frac{du}{dr} \quad \epsilon_{\theta\theta} = \frac{u}{r} \quad (\text{A.9})$$

$$\begin{bmatrix} \sigma_{rr} \\ \sigma_{\theta\theta} \\ \sigma_{zz} \end{bmatrix} = \frac{E}{(1+\nu)(1-2\nu)} \begin{bmatrix} 1-\nu & \nu & \nu \\ \nu & 1-\nu & \nu \\ \nu & \nu & 1-\nu \end{bmatrix} \begin{bmatrix} \epsilon_{rr} \\ \epsilon_{\theta\theta} \\ \epsilon_{zz} \end{bmatrix} - \frac{E\alpha\Delta T}{1-2\nu} \begin{bmatrix} 1 \\ 1 \\ 1 \end{bmatrix} \quad (\text{A.10})$$

$$\frac{d\sigma_{rr}}{dr} + \frac{1}{r}(\sigma_{rr} - \sigma_{\theta\theta}) + \rho_0 b_r = -\rho_0 \omega^2 r \quad (\text{A.11})$$

Substituting the equations A.9 and A.10 into A.11 show

$$\frac{\partial}{\partial r} \left\{ \frac{1}{r} \frac{\partial}{\partial r} (ru) \right\} = \frac{\alpha(1+\nu)}{1-\nu} \frac{\partial \Delta T}{\partial r} - \frac{(1+\nu)(1-2\nu)}{E(1-\nu)} \rho_0 (b + \omega^2 r) \quad (\text{A.12})$$

For a hollow cylinder subjected to number of conditions:

1. No body force acting on the cylinder
2. Zero angular velocity

3. Uniform Temperature

4. Different but uniform and constant pressure applied at the inner surface and the outer surface , denoted as  $p_i$  and  $p_o$  respectively

The right hand side of the equilibrium equation becomes zero,

$$\frac{\partial}{\partial r} \left\{ \frac{1}{r} \frac{\partial}{\partial r} (ru) \right\} = \frac{\partial^2 u}{\partial r^2} + \frac{1}{r} \frac{\partial u}{\partial r} - \frac{u}{r^2} = 0 \quad (\text{A.13})$$

that has a following general solution

$$u = Ar + \frac{B}{r} \quad (\text{A.14})$$

and substituting equation A.14 into equation A.10 shows that the radial stress,  $\sigma_{rr}$ , can be expressed as follows:

$$\begin{aligned} \sigma_{rr} &= \frac{E}{(1+\nu)(1-2\nu)} \left\{ (1-\nu) \frac{\partial u}{\partial r} + \nu \frac{u}{r} \right\} \\ &= \frac{E}{(1+\nu)(1-2\nu)} \left\{ A - (1-2\nu) \frac{B}{r^2} \right\} \end{aligned} \quad (\text{A.15})$$

If the pressure applied on the inner radius,  $r = r_i$  and the outer radius,  $r = r_o$  are defined as  $p_i$  and  $p_o$  respectively, the radial stress at those boundaries must be

$$\sigma_{rr}(r = r_i) = -p_i \quad \sigma_{rr}(r = r_o) = -p_o \quad (\text{A.16})$$

With three equations, A.14, A.15 and A.16 that defines both displacement and radial stress, the constant A and B can be solved:

$$A = \frac{(1+\nu)(1-2\nu)}{E} \frac{p_i r_i^2 - p_o r_o^2}{r_o^2 - r_i^2} \quad B = \frac{1+\nu}{E} \frac{r_i^2 r_o^2}{r_o^2 - r_i^2} (p_i - p_o) \quad (\text{A.17})$$

Hence the displacement field is

$$\vec{u} = \frac{(1 + \nu)r_i^2 r_o^2}{E(r_o^2 - r_i^2)} \left\{ \frac{p_i - p_o}{r} + (1 - 2\nu) \frac{p_i r_i^2 - p_o r_o^2}{r_i^2 r_o^2} r \right\} \vec{e}_r - \nu \epsilon_{zz} r \vec{e}_r + \epsilon_{zz} z \vec{e}_z \quad (\text{A.18})$$

For tracking the changes in the cross-sectional area of the vessel, we assume a plane parallel to the circular face dissecting a cylinder in half. For calculating the changes in the area, we assume that cylinder retains its circular shape and that it does not stretch out of plane; the circular cross-section is restricted to in-plane motion. This assumption leads to a case where plane strain,  $\epsilon_{zz}$ , is zero. Therefore, the displacement field becomes only dependent on  $r$  and the displacement field equation A.19 simplifies to

$$\vec{u} = \frac{(1 + \nu)r_i^2 r_o^2}{E(r_o^2 - r_i^2)} \left\{ \frac{p_i - p_o}{r} + (1 - 2\nu) \frac{p_i r_i^2 - p_o r_o^2}{r_i^2 r_o^2} r \right\} \vec{e}_r \quad (\text{A.19})$$

For area tracking due to external compression, we first assume that internal pressure is fixed. In this case, the cross-sectional area can be expressed as

$$A = \pi(r_i + u)^2 \quad (\text{A.20})$$

In this thesis, the outer radius is much greater than the inner radius, so  $r_o \gg r_i$  can be assumed and the displacement field can be approximated

$$\begin{aligned} \vec{u} &\approx \frac{(1 + \nu)r_i^2 r_o^2}{E r_o^2} \left\{ \frac{p_i - p_o}{r} + (1 - 2\nu) \frac{-p_o r_o^2}{r_i^2 r_o^2} r \right\} \vec{e}_r \\ &= \frac{(1 + \nu)r_i^2}{E} \left\{ \frac{p_i - p_o}{r} + (1 - 2\nu) \frac{-p_o}{r_i^2} r \right\} \vec{e}_r \end{aligned} \quad (\text{A.21})$$

By substituting (A.21) into (A.20)

$$\begin{aligned}
 A &= \pi r_i^2 \left\{ 1 + \frac{1+\nu}{E} \{(p_i - p_o) - (1-2\nu)p_o\} \right\}^2 \\
 &= \pi r_i^2 \left\{ 1 + \frac{1+\nu}{E} p_i - \frac{2(1-\nu^2)}{E} p_o \right\}^2
 \end{aligned} \tag{A.22}$$

Then the normalized area,  $\alpha$ , normalized to the cross-sectional area before compression can be calculated with the following expression

$$\alpha = \frac{A}{A_0} = \frac{\pi r_i^2 \left\{ 1 + \frac{1+\nu}{E} p_i - \frac{2(1-\nu^2)}{E} p_o \right\}^2}{\pi r_i^2 \left\{ 1 + \frac{1+\nu}{E} p_i \right\}^2} = \left\{ 1 - \frac{2(1-\nu^2)p_o}{E + (1+\nu)p_i} \right\}^2 \tag{A.23}$$